Hydrodynamics of Regional and Seasonal Variations in Congo Basin Precipitation

Kerry H. Cook and Edward K. Vizy

Department of Geological Sciences

The University of Texas at Austin

Austin TX

Reference: Cook KH, Vizy EK (2021) Hydrodynamics of Regional and Seasonal Variations in Congo Basin Precipitation. *Climate Dynamics,* DOI 10.1007/s00382-021-06066-3

ABSTRACT

The processes that determine the seasonality of precipitation in the Congo Basin are examined using the atmospheric column moisture budget. Studying the fundamental determinants of Congo Basin precipitation seasonality supports process-based studies of variations on all time scales, including those associated with greenhouse gas-induced global warming.

Precipitation distributions produced by the ERA5 reanalysis provide sufficient accuracy for this analysis, which requires a consistent dataset to relate the atmospheric dynamics and moisture distribution to the precipitation field. The Northern and Southern Hemisphere regions of the Congo Basin are examined separately to avoid the misconception that Congo Basin rainfall is primarily bimodal.

While evapotranspiration is indispensable for providing moisture to the atmospheric column to support precipitation in the Congo Basin, its seasonal variations are small and it does not drive precipitation seasonality. During the equinoctial seasons, precipitation is primarily supported by meridional wind convergence in the moist environment in the 800 hPa to 500 hPa layer where moist air flows into the equatorial trough. Boreal fall rains are stronger than boreal spring rains in both hemispheres because low-level moisture divergence develops in boreal spring in association with the developing Saharan thermal low. The moisture convergence term also dominates the moisture budget during the summer season in both hemispheres, with meridional convergence in the 850-500 hPa layer as cross-equatorial flow interacts with the cyclonic flow about the Angola and Sahara thermal lows. Winter precipitation is low because of dry air advection from the winter hemisphere subtropical highs over the continent.

Key words: Congo Basin rainfall; central Africa precipitation; African rainfall seasonality; African precipitation; Angola low; African precipitation processes; Saharan heat low

1. Introduction

Equatorial western and central Africa comprises the second-largest river basin on the planet, the Congo Basin, and the second-largest tropical forest. The Congo River Basin is nearly half the size of the continental U.S., and the region's tropical forest is the largest contiguous tract of forest in Africa (Shapiro et al. 2020). The most extensive peatland complex is also located here, underlying the swamp forests of the central Congo Basin and storing an estimated 30.6 Pg of carbon (Dargie et al. 2019). The basin boasts high numbers of aquatic, avian, and mammalian species, and the river provides about 30% of Africa's freshwater resources (Harrison et al. 2016).

Despite its size and importance on both local and global scales, precipitating systems are poorly understood and sparsely observed. The number of reporting stations has declined since the 1980s (Washington et al. 2013; Maidment et al. 2015; Nicholson et al. 2018), limiting opportunities to calibrate and evaluate satellite-based observations (Nicholson et al. 2019). The annual rainfall total is thought to be barely adequate for maintaining the tropical forest vegetation in most of the Congo Basin (Guan et al. 2015), suggesting a potential vulnerability to climate change.

Our understanding of the fundamental hydrodynamics of Congo Basin rainfall is incomplete on all scales, and this impedes our ability to develop confidence in observed and projected trends through physical attribution. Here we focus on regional space scales and climatological time scales to advance our fundamental understanding of the region's rainfall seasonality. We quantify the individual roles of evapotranspiration and atmospheric moisture convergence in supporting rainfall throughout the seasonal cycle in various regions, and identify the atmospheric processes that lead to regional and seasonal variations in precipitation.

Background on our current understanding of the hydrodynamics of Congo Basin rainfall is provided in the following section. Section 3 details the methodological approach, and the results are in section 4. Section 5 provides a summary and conclusions, including a discussion of the potential implications of the analysis for understanding observed and predicted greenhouse gas-induced climate change in the Congo Basin.

2. Background

The Congo Basin precipitation climatology is often described in the literature as being bimodal, but classification studies do not agree with this characterization. Using a 13-year satellite-observed rainfall climatology from TMPA (Huffman et al. 2007), Herrmann and Mohr (2011) classified rainfall seasonality regimes across Africa. A narrow band (2^{o}-3^{o} wide) along the equator extending from the Atlantic coast to the Rift Valley was identified as "humid". Nearly all of the remainder of the Congo Basin was found to have one wet season, with either one peak or two within a single rainy season, with the latter being more common in the eastern Congo Basin. Knoben et al. (2019) agree with these classifications expect they identify the narrow band along the equator as bimodal using harmonic analysis of the TMPA precipitation.

As is typical of tropical forest climates, the recycling of water between the evapotranspiration and precipitation fields provides significant support for precipitation in the Congo Basin throughout the year. Recycling ratios have been estimated in the 25% - 50% range (Pokam et al. 2012, Dyer et al. 2017, Sori et al. 2017). Crowhurst et al. (2021) note that basin-wide evaporation is lower in boreal fall than in boreal spring despite a similarity in precipitation due to lower leaf area indices and vapor pressure deficits in the southern rainforest.

The atmospheric circulation further supports Congo Basin rainfall through moisture transport and moisture convergence. During the solstitial months (December, January, February, June, July, and August), moisture convergence in central equatorial Africa occurs when cross-equatorial flow from the winter hemisphere tropics and subtropics into the summer hemisphere converges with cyclonic flow around the summer hemisphere thermal low (Cook and Vizy 2020). In the Northern Hemisphere, the Saharan thermal low migrates to the north through the spring and intensifies across the Sahara in summer (e.g., Lavaysse et al. 2009). In the Southern Hemisphere, The analogous feature in the Southern Hemisphere, the Angola low, is weaker and smaller than its Northern Hemisphere counterpart, but still recognized as a dominant feature of the summer climate (Howard and Washington 2018). This dynamics points to the southeastern Indian Ocean as a primary source of Congo Basin moisture during boreal summer, and the northeastern Indian Ocean during boreal winter.

During the equinoctial seasons, the primary moisture source for central equatorial Africa is southeasterly flow from the South Indian Ocean in association with the Southern Hemisphere component of the low-level Somali jet (Dyer et al. 2017; Cook and Vizy 2020).

Low-level westerlies from the equatorial Atlantic have also been suggested as an important moisture source for Congo Basin rainfall (Pokam et al. 2012, Dezfuli and Nicholson 2013), especially in boreal fall when the inflow is stronger than in boreal spring (Dyer et al. 2017). However, the Atlantic is a more minor source of moisture than the Indian Ocean (e.g., van der Ent and Savenijie 2013; Dyer et al. 2017; Cook and Vizy 2019). While Nicholson and Grist (2003) suggest that the South Atlantic anticyclone is instrumental in controlling onshore flow from the Atlantic, other studies associate it with a Walker (or Walker-like) circulation with rising over the Congo Basin and subsidence over the equatorial eastern Atlantic (Schwendike et al. 2014; Pokam et al. 2014; Cook and Vizy 2016; Zhao and Cook 2020; Longandjo and Rouault 2020).

Studies exploring the variability of Congo Basin rainfall help advance our understanding of connections to the large-scale circulation. Laing et al. (2011) find that convection is more widespread in the Congo Basin during active phases of the Madden-Julian Oscillation. On longer time scales, Dezfuli and Nicholson (2013) suggest that there is sensitivity on interannual time scales to global SSTs along the Atlantic coast and the eastern Congo Basin during the boreal fall rainy season. In a coupled GCM simulation with water tagging, Dyer et al. (2017) find that there is a northward shift of the primary moisture source from the southeastern Indian Ocean to the equatorial Indian Ocean during wet years in their simulation.

There is uncertainty in the literature about whether precipitation trends in the Congo Basin have been definitively detected. Malhi and Wright (2004) report a negative trend over the 1960-1998 period using the Climate Research Unit (CRU; New et al. 2000) rain gauge data. This dataset is based on a network of ground-based observing stations that are not well distributed through the Congo Basin [Fig. 2 in Malhi and Wright (2004)]. An examination of trends in eight precipitation datasets for 1983-2010 by Maidment et al. (2015) finds disagreement among them over Central Africa. Along with Dinku et al. (2018), they express concern that apparent drying occurs in blended satellite-gauge datasets because of the ongoing negative trend in the number of reporting stations in the Congo Basin. Nicholson et al. (2018) focus on the regionality of trends in analyzing rain gauge measurements for 1921-2014. They find positive trends significant at the 90th percentile at 5ºN - 10ºN in boreal spring, but negative trends elsewhere that are not uniformly significant.

Cook and Vizy (2020) examine trends in Congo Basin rainfall in six observational datasets and find a statistically-significant decline in annual rainfall over the 1979-2017 time period in all datasets, with strongest trends from March through August. They associate the drying with a mechanism that could plausibly be associated with greenhouse gas-induced global warming, namely, poleward shifts of the continental thermal lows. However, they also find that the observed trends are generally weaker and less significant over the more recent 1998-2017 time period, especially in boreal spring. An exception is the boreal summer when robust trends persist in association with the observed, greenhouse gas-induce strengthening and northward shift of the Saharan thermal low (Cook and Vizy 2015, Vizy and Cook 2017).

Studies of Congo Basin vegetation and ecosystems are more consistent in suggesting decline, although causes are unclear. Zhou et al. (2014) examine vegetation indices over the 2000-2012 and find a browning trend in the Congo Basin for boreal spring. A connection with precipitation observations is tenuous, however, since only one precipitation dataset is examined and the anomalies are not statistically significant. Shapiro et al. (2021) estimate that less than 70% of the Congolese rainforest remains intact, which is a decrease from 78% in 2000.

Evaluation and attribution of observed trends is hampered because we currently do not have a thorough understanding of how the basic precipitation climatology of the Congo Basin works. Developing confidence in projections is also impeded by this lack of knowledge, along with poor performance by coupled GCMs (Creese and Washington 2016, 2018; Crowhurst et al. 2020) and regional-model intercomparison projects (e.g., Tamoffo et al. 2020) in the Congo Basin, and disagreement among model projections (e.g., Christensen et al. 2013).

In this paper, we present a basic analysis of the Congo Basin rainfall climatology with attention to regionality and seasonality, using the constraints of the column moisture budget to understand connections to regional evapotranspiration and the larger-scale atmospheric hydrodynamics. Such an analysis will be useful for evaluating model simulations at the process level, and for interpreting and attributing any observed and simulated changes in Congo Basin precipitation.

3. Methodology

The primary analysis region is 10ºS to 10ºN and 10ºE to 30ºE. This region is shown by the red box in Figure 1a along with topography (shaded). Low points in the analysis region are the coastal plains along the Atlantic and in central equatorial Africa near 17ºE. Elevations increase to 600 m east of the Atlantic coastal plains and well over 2000 m in the Rift Valley region that bounds the analysis region on the east. The Congo River and its many tributaries form a dense network throughout the areas with elevations under 600 m (dark blue area).

The analysis region is not identical to the Congo River Basin, which is the sedimentary basin of the Congo River, because our focus is on atmospheric processes. This hydrologic basin extends to 6ºN - 8ºN over the Central African Republic, and to 12ºS - 13ºS over northern Angola, southern Democratic Republic of Congo, and northeastern Zambia. We use the term "Congo Basin" here for convenience, since the hydrologic basin overlaps substantially with the analysis region and referring to "equatorial central and western Africa" is cumbersome.

The analysis region is also not coincident with the Congo tropical forest. The dark green shading in Fig. 1b indicates tropical forest vegetation in Africa as specified in the ERA5 reanalysis, showing that much of this ecosystem type in Africa is located in the Congo Basin.

The primary dataset for this analysis is the ECMWF Reanalysis 5 (ERA5; Hersbach et al. 2020), which provides hourly estimates of a large number of atmospheric, land, and ocean climate variables at 0.25º resolution (30 km grid) on 137 vertical levels. While the ERA5 dataset extends back to 1950, we use only values from the satellite era, forming a climatology by averaging from 1979 to 2020. We choose this source for evaluating the modeled hydrodynamic fields (e.g., winds, geopotential heights, temperature, and moisture) because of its high resolution and good performance in other regions of Africa, albeit with direct observations that are less sparse than the Congo Basin (e.g., Vizy and Cook 2019; Danso et al 2019).

We also use precipitation and evapotranspiration fields from ERA5. For precipitation, which has been less reliable in prior generations of reanalyses, we evaluate the ERA5 climatology through comparison with the following observational datasets:

- ARC2 (0.1º resolution; Novella and Thiaw 2013); averaged 1983 – 2020
- CHIRPS2 (0.05º; Funk et al. 2015); averaged 1981 – 2020
- CMORPH (8 km resolution; Joyce et al. 2004); averaged 1998 – 2019
- IMERG (0.1º resolution; Huffman et al. 2018); averaged 2001 – 2020
- PERSIANN-CDR (0.25º; Sorooshian et al. 2000); averaged 1983 – 2020
- TAMSAT (4 km; Maidment et al. 2017); averaged 1983 – 2020
- TRMM TMPA (0.25º resolution; Huffman et al. 2007); 1998 – 2019

The years averaged to form climatologies vary slightly among the datasets due to their availabilities.

In the ERA5 reanalysis, evapotranspiration values are calculated within a land surface model component in the absence of daily observed distributions for assimilation. This model, known as HTESSEL (Balsamo et al. 2009), is an update to the TESSEL land surface model (e.g., Viterbo and Beljaars 1995) and tracks surface water through 4 vertical layers. In addition to vertical percolation, the model accounts for surface runoff and drainage with dependence on local topography and soil type. It divides each grid box at the surface into sub-grids known as tiles to capture the effects of smaller-scale surface inhomogeneities such as soil texture and vegetation. Two types of vegetation, high and low, are specified along with their areal coverage and each vegetation type is assigned characteristics such as canopy resistance and leaf area index. In regions where an evaluation of surface and near-surface variables in ERA5 has been possible, large improvements compared with previous reanalyses have been reported (e.g., Betts et al. 2019; Johannsen et al. 2019). Crowhurst et al. (2021) evaluate a reanalysis production, ERA5-Land, that is closely related to the ERA5 reanalysis. In a comparison with the LandFlux-EVAL dataset (Mueller et al. 2013), they find that ERA5-Land slightly overestimate the seasonal cycle of evaporation by less than 1 mm/day.

Using precipitation and evapotranspiration values from ERA5 allows us to use reanalysis values consistently in the atmospheric moisture budget calculation. This calculation is used to quantify the roles of evapotranspiration and the vertically-integrated moisture flux convergence in supporting rainfall in different seasons and regions, and to understand relationships with the larger-scale atmospheric circulation. For a climatology, assuming there is no accumulation of water vapor, conservation of water mass in an atmospheric column requires that

$$P = E - \frac{1}{g\rho_W}\int_{p_S}^{0}\left[\nabla\cdot\left(q\vec{V}\right)\right]dp\ , \qquad (1)$$

where P is precipitation, E is evapotranspiration, ρ_W is the density of water vapor, q is specific humidity, and $\vec{V}$ is the 3-dimentional wind velocity. E is often interpreted as a “recycling” of moisture from the land surface. The second term on the right-hand-side of Eq. 1 is the vertically-integrated moisture flux convergence, M, which can be further decomposed into the sum of the vertically-integrated horizontal moisture convergence (C), the vertically-integrated horizontal moisture advection (A), and the orographic uplift (O) terms as follows:

$$C = -\frac{1}{g\rho_W}\int_{p_S}^{0}\left[q\nabla\cdot\vec{V}\right]dp\ , \qquad (2)$$

$$A=-\frac{1}{g\rho_W}\int_{p_S}^{0}\left[\vec{V}\cdot\nabla q\right]dp\ , \tag{3}$$

and

$$O=-\frac{1}{g\rho_W}\left(q\omega\right)_s . \tag{4}$$

C captures support of a precipitation field by wind convergence in the moist environment. The advection term, *A*, measures contributions when the wind transports moisture in the presence of specific humidity gradients. *O* captures the effects of orographic uplift. Defining the product of the specific humidity and vertical p-velocity at the surface in Eq. 4 is problematic because of their typical correlation on time scales of seconds and uncertainty in defining the surface vertical velocity, so *O* is calculated as a residual and collects numerical error due to the necessity of expressing the vertical integrals in Eqs. 2 and 3 as discrete sums and using finite differencing to express derivatives.

4. Results

a. Evaluation of ERA5 precipitation

Caution is appropriate when using precipitation fields from reanalyses because rainfall values are not assimilated. In this case, we are motivated to use the ERA5 reanalysis precipitation fields in the moisture budget analysis (Eqs. 1 - 4) for internal consistency. We carefully compare the precipitation climatology from ERA5 with observational datasets before proceeding with the analysis.

Figure 2 shows daily precipitation values averaged from 10ºE-30ºE over three latitudinal ranges, namely, 0º-5ºN (Fig. 2a), 5ºS-0º (Fig. 2b), and 5ºS-5ºN (Fig. 2c) in the ERA5 reanalysis (red line) and seven observed climatologies (see section 3). In the 0º-5ºN latitude band (Fig. 2a), precipitation maxima in April and October are separated by a boreal summer period in which rainfall rates are maintained above 4 mm/day. There is a single drier period in boreal winter when rainfall rates are 1-2 mm/day, and highest rainfall rates occur in October.

Rainfall seasonality in the 5ºS-0º latitude band (Fig. 2b) is similar, with a single dry period in austral winter and a long rainy season with two peaks. As in the 0º-5ºN latitude band (Fig. 2a), highest rainfall rates are in boreal fall, but in November not October as in the Northern Hemisphere.

As a point of comparison with other studies we also include an average from 5ºS to 5ºN in Fig. 2c. However, choosing this averaging region gives the mistaken impression that Congo Basin rainfall is characteristically bimodal. It is not, with the possible exception of a narrow region along the equator, depending on how one defines the term "bimodal". (see section 2). The spurious bimodal pattern arises when the averaging regional spans the equator.

Differences among the observational datasets are about 1 mm/day or less, and precipitation averages in the ERA5 climatology are similar to the observational datasets. The greatest difference occurs in January, when ERA5 precipitation is about 1 mm/day higher than observed. ERA5 rainfall is also slightly (less than 1 mm/day) outside the observed range in August and September in the Southern Hemisphere Congo Basin. Overall, however, the areal averages suggest that the ERA5 reanalysis captures the seasonality and magnitude of Congo Basin precipitation well.

Four months with maximum and minimum rainfall according to Fig. 1 – January, April, July, and October - are chosen for a regional comparison of the ERA5 precipitation with various observational datasets, shown in Figures 3 and 4. In January, small-scale precipitation maxima form along the equatorial Atlantic coast and the Rift Valley foothills, with a continental-scale precipitation maximum south of 5ºS (Fig. 3a). Precipitation rates are fairly uniform at 4-5 mm/day from 7ºS to 2ºS, with strong meridional gradients and precipitation reductions from 2ºS to 5ºN. January rainfall rates are very low north of 5ºN in boreal winter.

The equatorial maxima in the east and west remain in April (Fig. 3b), and there is a broad region between them from about 8ºS to 5ºN with uniform rainfall rates of 5 mm/day. Note the hemispheric asymmetry in the location of the regions of strong meridional precipitation gradients to the north and south of this region; the region of uniform precipitation extends farther into the Southern Hemisphere than into the Northern Hemisphere.

In the July precipitation distribution (Fig. 3c), a pronounced meridional precipitation gradient is located near the equator, with opposite sign to January's gradient. The precipitation maximum is 5º-10º off the equator and located west of 20ºE along the Guinean coast and Cameroon highlands, in contrast to January (Fig. 3a) when the precipitation maximum is farther off the equator (largely outside of the analysis region) and more widespread.

Rainfall rates in October (Fig. 3d) are greater than in April (Fig. 3b) throughout the Congo Basin, and the region of uniform rainfall extents farther north and south. The enhancements along the Atlantic coast and the eastern topography are also stronger.

In the remaining figure panels of Fig. 3, and those of Fig. 4, the distinguishing features of the seasonally-varying precipitation field as represented in ERA5 (Fig. 3a – d) are replicated. There are certainly some variations among the datasets, but this would be expected with any set of observed precipitation climatologies. We conclude that the ERA5 reanalysis climatology produces a good representation of the Congo Basin precipitation distribution both regionally and seasonally, sufficient for use in the moisture budget analysis.

b. Seasonal cycle of precipitation: Roles of evapotranspiration and atmospheric moisture convergence

To gain a first-order quantitative understanding of the relative importance of evapotranspiration and atmospheric moisture convergence in supporting rainfall throughout the annual cycle, we average from 10ºE to 30ºE in swaths that are 5º of latitude wide (10ºS-5ºS, 5ºS-0º, 0º-5ºN, and 5ºN-10ºN).

Figures 5a-e display the seasonal cycles of precipitation (*P;* blue lines) and evapotranspiration (*E;* red lines) from the ERA5 climatology averaged over various latitudinal ranges. When $P > E$ the vertically-integrated moisture flux convergence is positive and when $P < E$ it is negative and there is moisture divergence in the atmospheric column (Eq. 1). These times are indicated by *C* and *D*, respectively, in Figs. 5a-d. Green dashed lines in Figs. 5a-d are skin temperature.

In the northern Congo Basin (5ºN-10ºN, Fig. 4a) there is a single rainy season. Precipitation exceeds 3 mm/day from April through October and peaks at 7.8 mm/day in August. There is very little precipitation in December, January, and February. Evapotranspiration rates are more constant than precipitation rates, ranging from 1.6 mm/day in January to 3.8 mm/day in September and October. The atmosphere converges moisture into this latitude band from April through October, but in November, December, and January moisture diverges out of the region. The seasonal cycle of evapotranspiration is in phase with precipitation but out of phase with surface temperature, with warmest temperatures during the dry season.

There is also a single rainy season in the 0º-5º latitude band (see Figure 2a), but with two maxima (Fig. 5b). Evapotranspiration and surface temperature are quite constant throughout the year. Atmospheric moisture convergence prevails except during the dry season in December and

January, so some of the water that evaporates from the surface is carried out of the region during boreal winter.

The moisture balance is similar in the 5ºS-0º averaging band (Fig. 5c), with a shift in seasons. Evapotranspiration and surface temperature do not vary much through the year. Moisture converges in the atmospheric column during the long wet season and diverges during the short austral winter dry season.

In the 10ºS-5ºS band (Fig. 5d), low rainfall prevails from May through much of August, and the atmosphere diverges moisture out of the region from mid-April until September. Similar to the 5ºN-10ºN latitude band (Fig. 5a), there is a single rainy season with precipitation supported about equally by evapotranspiration and atmospheric moisture convergence.

Precipitation and evapotranspiration time series averaged over the entire analysis region (10ºS-10ºN; solid lines) and a central Congo Basin region (5ºS-5ºN; dashed lines) are shown in Fig. 5e. These are averaging regions often used in the literature and, as discussed above, lead to the false conclusion that the Congo Basin rainfall is bimodal. In addition, using these averaging regions that span the equator suggests that atmospheric moisture divergence never occurs, since $P > E$ at all times in this averages. As seen in Figs. 5a-d, this is not a correct conclusion because few, if any, locations experience bimodality in rainfall.

To further examine the regionality of the hydrodynamics of Congo Basin rainfall, Figure 6 displays maps of precipitation, evapotranspiration, and the vertically-integrated moisture flux convergence for the four months representing high and low precipitation rates, namely, January, April, July, and October.

In January, rainfall maxima occur along the equatorial Atlantic coast, the Rift Valley topography, and the southern edge of the domain (Fig. 6a). In contrast, the evapotranspiration maximum is in the center of the Congo Basin on the equator (Fig. 6b); the regional precipitation maxima are off the equator due to atmospheric moisture convergence (Fig. 6c). In the winter hemisphere, low rainfall rates are related to large-scale atmospheric moisture divergence, while the negative meridional gradient between the equator and 10ºN is associated with the evapotranspiration gradient. Precipitation enhancements in the far east and west of the analysis domain are associated with atmospheric moisture convergence.

In April, precipitation maxima along the equatorial Atlantic coast and the Rift valley on the edge of the analysis domain persist, and the rest of the Congo Basin receives relatively uniform rainfall from 8ºS to 6ºN (Fig. 6d). Evapotranspiration (Fig. 6e) is a little stronger than in January, but still centered on the equator. The atmospheric moisture convergence field closely resembles the precipitation distribution (Fig. 6f).

The moisture budget in July (Figs. 6g-i) is similar to that in January (Figs. 6a-c) reflected across the equator. However, the Atlantic coast maximum near 2ºS in January is replaced by a maximum north of the Cameroon Highlands near 6ºN and the precipitation enhancement in the east is smaller. Rainfall rates in the tropical Northern Hemisphere (0º to 5ºN) in July are about 1 mm/day less than in the tropical Southern Hemisphere (0º to 5ºS) in January because evapotranspiration rates are lower (Fig. 6h). The pattern of atmospheric moisture divergence in the winter hemisphere with convergence in the summer hemisphere reoccurs (Fig. 6i).

October rainfall (Fig. 6j) is similar in distribution to April rainfall (Fig. 6d) but rainfall rates are higher because the atmospheric moisture convergence is greater; evapotranspiration rates are similar in April and October (see also Figs. 5b and c)

Overall, Figs. 5 and 6 show that while evapotranspiration (water recycling) provides an important source of moisture for precipitation throughout the year in the Congo Basin, it is not primarily responsible for the seasonality of rainfall; seasonality is determined largely by the atmospheric hydrodynamics. During the solstitial seasons there is column moisture divergence in the winter hemisphere ($E > P$) and convergence ($P > E$) in the summer hemisphere. Depending on latitude, evapotranspiration exceeds precipitation by more than 50% in the winter hemisphere during the solstitial months. During the equinoctial months, precipitation exceeds evapotranspiration by up to 70%.

In the following section, the vertically-integrated moisture convergence flux is decomposed to understand the circulation features and specific humidity distributions that determine the seasonality of Congo Basin rainfall. Since there are similarities between the equinoctial seasons, they are investigated together in the following section. Analysis of the hydrodynamics of the solstitial seasons follows.

c. Equinoctial seasons

Figures 7a-c display the vertically-integrated convergence (C; Eq. 2), advection (A; Eq. 3), and orographic (O; Eq. 4) components of the vertically-integrated moisture flux convergence for the April climatology. The largest overall contribution to moisture flux convergence in the atmospheric column is from the convergence term (Fig. 7a), which exhibits some small-scale waviness due to finite differencing. An annulus pattern emerges with stronger values of C on the perimeter of the central Congo Basin. The vertically-integrated advection term (Fig. 7b) generally supports moisture flux convergence in the central Congo Basin, adding to the C term, and it opposes the C term in the perimeter region except in the Northern Hemisphere. However, the A term is weaker than the C term throughout the region.

The O term is primarily negative, opposing the C term in the Northern and Southern Hemisphere perimeter regions. Since large values of O occur away from the region's topographic features (Fig. 1a), we interpret it as primarily numerical error due to finite differencing and the monthly sampling of variables used to calculate the nonlinear *C* and *A* terms (Eqs. 2 and 3). In particular, for the April case, *O* is large and negative in opposition to the *C* term (Fig. 7a) from 5ºN-10ºN and 5ºS-10ºS, capturing in part numerical error in the divergence calculation (Eq. 2). Physical interpretation of this term is, therefore, limited.

In October (Figs. 7d-f), the *C* term is again dominant. Positive values in the perimeter region are similar to those for April (Fig. 7a), while values are larger in the central Congo Basin region. The advection term (Fig. 7e) provides no support for rainfall in the central region. The orographic term (Fig. 7f) is also weaker than in April (Fig. 7c) in most of the basin, but strong and positive on the eastern and western edges of the analysis region. These figures show that the higher rainfall rates of the boreal fall season compared with boreal spring (Figs. 2-4) are primarily associated with the convergence term.

To relate the vertically-integrated moisture budget components with the atmospheric hydrodynamics, the core expressions of the vertically-integrated *C* and *A* terms on individual levels ($-q\nabla\cdot\vec{V}$ and $-\vec{V}\cdot\nabla q$, respectively) are examined. The 900 hPa and 750 hPa levels are chosen as representative.

April values of the convergence term at 900 hPa are shown in Figure 8a along with moisture transport vectors ($q\vec{V}$) to aid interpretation. Positive values of the *C* term in the perimeter region occur near the surface (900-800 hPa) with the exception of the far east (30ºE) where the topography rises above 850 hPa. At and below 900 hPa, $-q\nabla\cdot\vec{V}$ is negative in the central Congo Basin, in contrast to the vertically-integrated C term which is positive (Fig. 7a). The vectors indicate that the strong convergence at 5Nº-10ºN is paired with the divergence in the central Congo Basin as the meridional moisture transport increases with latitude from 5ºS to 5ºN. Moisture convergence in the west (~15ºE) is associated with moisture divergence along the Atlantic coast, and in the south (5ºS-8ºS) with southeasterly flow.

Positive moisture convergence over the central Congo Basin is present in a deep layer from 800 hPa to 500 hPa, represented by the 750 hPa level in Fig. 8b. This convergence overlies low-level divergence (Fig. 8a) and is a primary support for rainfall from about 7ºS to 8ºN across the breadth of the Congo Basin. At this level the flow is easterly close to the equator, with northeasterlies north of about 5ºN and southeasterlies south of 5ºS, so the positive values of moisture convergence are associated with meridional convergence.

Low-level convergence terms and moisture transport vectors in October (Fig. 8c) differ from those in April (Fig. 8a). Moisture is transported eastward across the central Congo Basin where it converges near the topography in the far eastern Congo Basin. Areas of low-level moisture divergence and convergence are scattered over the central basin; a counterpart to the low-level meridional divergence seen in April (Fig. 8a) does not occur. These differences in the low-level moisture convergence and transport are a primary reason for stronger precipitation in October than April.

At higher levels, moisture transport in October (Fig. 8d) is similar to April (Fig. 8b). Meridional convergence in the austral spring Southern Hemisphere is weaker than that in the boreal spring Northern Hemisphere at 750 hPa, but stronger at 600-700 hPa (not shown).

The advection terms evaluated on individual levels are small (not shown). They exceed 1 x 10^{-3} s^{-1} only locally along the Rift Valley topography, primarily outside of the analysis domain. This indicates that moisture gradients do not play an important role in the hydrodynamics of Congo Basin rainfall during spring and fall; specific humidity values are relatively uniform across the analysis region. For example at 850 hPa, specific humidity values range from 13 - 15 x 10^{-3} kg-H_2O/kg-air across the analysis domain during the equinoctial seasons with no strong gradients.

To relate the moisture budget analysis to the large-scale circulation, the atmospheric dynamics is examined on a larger domain. Figure 9a shows 900 hPa winds and geopotential heights from the ERA5 April climatology. The low-level pattern of moisture convergence between 6ºN and 10ºN with moisture divergence to the south over the central Congo Basin (Fig. 8a) is associated with a region of low geopotential heights centered near 12ºN over the central and eastern Sahel. This is the thermal low (the Saharan low) that develops over northern Africa each spring. It strengthens during boreal spring, moving northward and expanding westward. In April, the low-latitude, low-level winds flow down the geopotential height gradient causing divergence over the central Congo Basin from 5ºS to 7ºN, with convergence to the north. Note that the westerly wind on the west coast near the equator is part of this down-gradient flow; it is not connected with the South Atlantic high which is far from the region in April, centered west of the Greenwich meridian at 30ºS (see Fig. 1 in Sun et al. 2017).

Consistent with Figs. 8a and c, the low-level dynamics is different in October compared with April. Figures 9b and c show the 900 hPa and 850 hPa winds and geopotential heights for October; the 850 hPa level is included to clear the southern Africa topography. The thermal low that is analogous to the Saharan low - the Angola low – is the closed low near 15ºS at 850 hPa (Fig. 9c). It is weaker and smaller than the Saharan low because of the smaller zonal width and elevated-plateau topography of the continent in the Southern Hemisphere. It is associated with cyclonic circulation south of the equator at 900 hPa (Fig. 9b), but it does not lead to moisture divergence over the central Congo Basin in sharp contrast to April. Again, westerlies over the west coast are related to continental geopotential height gradients and they are not associated with the South Atlantic high.

At 800 hPa and above, represented by the 750 hPa level for April and October in Figures 10a and b, respectively, the meridional convergence that supports the deep layer of moisture convergence is evident. In the Northern Hemisphere tropics during both April and October, northeasterly flow originates in the subtropics over land and, in April only, the northern Indian Ocean. In April, the flow north of 10ºN over the Sahel is northerly/northeasterly along the eastern flank of the developing Saharan high. In October the inflow is from the northeast in association with both the Saharan and Arabian highs. Winds are close to geostrophic north of about 12ºN and develop a down-gradient orientation closer to the equator, supplying the meridional convergence that supports central Congo Basin rainfall in boreal spring.

In the Southern Hemisphere, during both boreal and austral spring (Figs. 10a and b), southeasterly flow originates over the southwestern tropical Indian Ocean. South of 10ºS, the flow is mostly geostrophic with lower geopotential heights over the equatorial Indian Ocean to the northeast and higher continental geopotential heights to the southwest. As the southeasterly flow crosses onto the African continent at 5ºS-10ºS, it develops an ageostrophic component directed into the equatorial trough and, as a result, meridional moisture convergence.

d. Solstitial seasons

Rainfall distributions in the central Congo Basin (5ºS to 5ºN) are characterized by strong meridional gradients during the solstitial seasons (Figures 3 and 4), with higher rainfall rates in the summer hemisphere and lower rates in the winter hemisphere. In the vertical integral, moisture convergence in the atmospheric column is confined primarily to the summer hemisphere with divergence in the winter hemisphere (Figs. 6c and i). The evapotranspiration maximum remains centered on the equator but drops off sharply poleward of 5º latitude in the winter hemisphere (Figs. 6b and h).

Figure 11 decomposes the vertically-integrated moisture flux convergence into convergence (*C*), advection (*A*), and orographic/residual (*O*) terms (Eq. 2-4). In January, the *C* term is largely positive south of about 7ºN, with negative values to the north (Fig. 11a). High values of the vertically-integrated moisture convergence (and rainfall) over the western equatorial Congo Basin and west of the Rift Valley topography are associated with this term. The *A* term (Fig. 11b) is strong and negative from 2ºN to 8ºN. In the summer hemisphere, the A term is small, and this difference explains why winter is dry while relatively high precipitation levels are maintained through the summer season (see Figs. 2-5). The *O* term (Fig. 10c) contributes weak moisture divergence in the central Congo Basin, and essentially cancels the negative values of the convergence term north of 6 ºN.

The three components of the vertically-integrated moisture convergence in July (Figs. 11d-f) are similar to those in January, but reflected about the equator. The primary difference between January and July is that the advection term is weaker in the Southern Hemisphere in July, and tilts from the southwest to the northeast.

Examining the core expression of the C term ($-\nabla \cdot q\vec{\ }$) at individual levels reveals partial cancellation between lower levels (850 hPa and below) and middle levels (800 hPa-600 hPa) in the winter hemisphere. Figures 12a and b provide examples at 900 hPa and 750 hPa, respectively, for the January climatology, and Figs. 12c and d for July. In January, high positive values at 900 hPa centered 5º off the equator in the winter hemisphere are cancelled in the vertical integral by negative values aloft. A similar pattern occurs in July in the winter hemisphere, but centered a few degrees farther poleward. In middle levels, exemplified by the 750 hPa level in Figs. 12b and d, the C term is positive, providing primary support for the positive vertically-integrated moisture convergence (Figs. 11a and d) and precipitation (Figs. 2 and 3) near the equator and into the summer hemisphere. The moisture transport vectors indicate that the negative regions off the equator in the winter hemisphere are coupled with these positive regions.

The winter hemisphere regions with a large negative advection term (*A*) also exhibits vertical structure. Figures 13a and b show $-\vec{V} \cdot \nabla q$ at 900 hPa and 750 hPa in January, respectively. Negative values between 5ºN and 10ºN at 900 hPa (Fig. 13a) mark a region of dry air advection that is slightly north of the region of low-level moisture convergence (Fig. 12a). However, without compensation aloft (Fig. 13b), this low-level dry air advection contributes to the vertically-integrated moisture divergence in the winter hemisphere (Figs. 6c and 11b). At 750 hPa (Fig. 13b), dry air advection extends from the equator to about 7ºN, overlying moist advection at 900 hPa (Fig. 13a) associated with inflow from the west.

For July, the 900 hPa advection term (Fig. 13c) indicates that topography plays a role in the southwest-to-northeast tilt of the region of vertically-integrated dry air advection (Fig. 11e). Low-level moist advection from the west near 5ºS is associated with westerly moisture transport and, at 750 hPa (Fig. 13d), a large region of dry air advection is associated with the southeasterly moisture transport.

January 900-hPa geopotential heights (shaded), specific humidity (contours), and winds (vectors) are plotted in Figure 14a on a larger domain. Note the strong meridional specific humidity gradient at 5ºN-10ºN. The northeasterly flow that is associated with a positive moisture convergence term and a negative moisture advection term between 5ºN and 10ºN (Figs. 12a and 13a) originates in the anticyclonic flow about the winter subtropical high over northern Africa. South of about 10ºN the wind becomes more ageostrophic and flows into the broad thermal low over the central Congo. With northerly winds ($v < 0$) and a negative meridional specific humidity gradient ($\partial q / \partial y < 0$), $-v \, \partial q / \partial y$ is negative. The meridional flow is importing dry subtropical air from the Sahara and Sahel, suppressing precipitation from 5ºN-10ºN in boreal winter (see Figs. 2-4). On the synoptic scale, this mechanism manifests as dry, cold air intrusions (Vizy and Cook 2009, 2014).

High positive values of the *C* term in the shallow near-surface layer (Fig. 12a) are also associated with this northerly flow but, as see in Fig. 12b, the moisture convergence term is negative in the layers immediately above. Figure 14b shows that at 750 hPa, a weaker flow continues southward after rising from the 900 hPa level. There is a band of upward vertical p-velocity between 5ºN and 10ºN with negative velocities up to 4 Pa/s in magnitude in the 850-750 hPa layer (not shown).

A similar dynamics occurs in July, but modified due to the southern Africa topography and smaller zonal extent of the continent. Since much of the southern Africa plateau extends above the 900 hPa level (see Fig. 14a), low-level geopotential heights (shaded), specific humidity (contours), and winds (vectors) are shown at 850 hPa in Fig. 15. The continental subtropical high is centered at 25ºS, farther south than its Northern Hemisphere counterpart (compare with Fig. 14a), and it is weaker and smaller. Nonetheless, a strong positive meridional specific humidity gradient develops over the southern Congo Basin (10ºS-5ºS) with equatorward dry air advection (Fig. 12c).

5. Summary and Conclusions

Clarifying our understanding of current and potential changes in Congo Basin climate, and the consequences for ecosystems, requires that we develop a deeper understanding of the hydrodynamic processes that support regional precipitation and determine its seasonality. This paper contributes to developing that understanding by evaluating the regional column moisture budget in the ERA5 reanalysis. The good accuracy of precipitation distributions produced by the ERA5 reanalysis on climatological time scales (Fig. 2 and 3) provides the opportunity to evaluate the atmospheric column moisture budget in a consistent dataset, in which the atmospheric dynamics and moisture distribution can be related to the precipitation field.

An examination of regional precipitation distributions dispels the notion that the Congo Basin can be described as a bimodal rainfall regime. This point was made by the classification studies of Herrmann and Mohr (2011) and Knoben et al. (2018) as well, but the description of Congo Basin rainfall seasonality as bimodal persists in the literature. The mistaken impression of bimodality occurs when inhomogeneous averaging regions that cross the equator are chosen. Even within 5º of latitude of the equator, the only dry season is the winter season which, of course, occurs in different months depending on the hemisphere, so averaging produces a bimodal pattern that is not realized locally. The equinoctial and summer seasons are the wettest, with maxima in spring and fall. Summer rainfall rates are 15% - 40% lower than the equinoctial maxima.

The atmospheric column moisture budget analysis (Eq. 1) shows that evapotranspiration is indispensable for providing moisture to the atmospheric column to support precipitation in the Congo Basin, as is typical in tropical forest regimes. However, seasonal variations in evapotranspiration are small and they do not drive precipitation seasonality. In averaging regions that are 5º wide in latitude running longitudinally across the Congo Basin, evapotranspiration rates exceed precipitation rates during the winter season in both hemispheres and the atmosphere diverges moisture out of the overlying column (see Fig. 5). In the equinoctial and summer seasons, precipitation exceeds evapotranspiration by 50% - 225%, depending on season and location, and moisture is converging in the atmospheric column.

The atmospheric hydrodynamics determines the seasonality, and much of the regionality, of Congo Basin rainfall. During the equinoctial seasons, precipitation is primarily supported by wind convergence in the moist environment (the *C* term in the column moisture budget, Eq. 2); specific humidity gradients are small so moisture advection (the *A* term in the column moisture budget, Eq. 3) is not effective (Fig. 7). In both boreal and austral spring, a deep layer of convergence extends from 800 hPa to 500 hPa to provide the primary support for rainfall within about 8º of the equator (Figs. 8b and d). During both equinoctial seasons, this convergence is primarily meridional in association with the equinoctial, large-scale geopotential height patterns that place low heights on the equator in the central Congo Basin (Fig. 10).

The low-level hydrodynamics is different between the two equinoctial seasons (e.g., April and October; Fig. 8). Moisture divergence in the central Congo Basin (5ºS to 5ºN) occurs at and below 900 hPa as southerly low-level winds flow down the geopotential height gradient toward the developing Saharan thermal low centered near 12ºN in April (Fig. 9). In October, the Southern Hemisphere counterpart – the Angola low – is weaker and less extensive than the Saharan low due to the smaller continental width and the southern Africa topography, so a similar dynamics does not develop. Instead, westerly flow into a broad equatorial trough develops, but the associated convergence is confined to the eastern Congo Basin. Because the low-level moisture divergence does not develop in October, it is the wetter of the two equinoctial rainy seasons in both hemispheres (see Figs. 2 and 5).

Similar to the equinoctial seasons, the moisture convergence term dominates the column moisture budget during the summer season in both hemispheres, with convergence in the 850-600hPa layer of southwesterlies in the Northern Hemisphere (e.g., July; Fig. 12d) and northeasterlies in the Southern Hemisphere (January; Fig. 12b). This cross-equatorial flow is the trade winds but modified over the continent, with higher magnitudes and a more meridional orientation, because of high geopotential heights over the winter hemisphere subtropics and lows over the summer hemisphere subtropics (Figs. 14b and 15b). Convergence occurs in the summer hemisphere when this cross-equatorial flow interacts with the cyclonic flow about the thermal lows.

Summer and winter rainy seasons are different, with the winter season much drier, because the advection term is large and negative in the winter season (Fig. 13). Anticyclonic flow about the Saharan high becomes ageostrophic south of about 10ºN, advecting dry air across a strong negative specific humidity gradient centered near 5ºN (Fig. 14). The dynamics is similar in Southern Hemisphere, also with equatorward dry air advection (Fig. 15).

The coupling between the subtropical thermal lows over the Africa continent and atmospheric moisture convergence over the Congo Basin was related to a mechanism for Congo Basin drying in Cook et al. (2020). Intensification, changes in seasonality, and/or shifts in the thermal lows in response to increasing greenhouse gas levels will have repercussions for Congo Basin rainfall.

In this paper we provide a basic understanding of the hydrodynamics of seasonality and regionality of Congo Basin rainfall. We show that Congo Basin rainfall seasonality and regionality is not locally driven by, for example, evaporation/evapotranspiration and surface temperature variations but by the atmospheric hydrodynamics including important tropical/subtropical interactions over the Africa continent and the Indian Ocean. Studying these fundamental determinants of the precipitation climatology will support process-based studies of variations on all time scales, including those associated with greenhouse gas-induced global warming. It is only through a process-level understanding that confident and useful projections of climate change in the Congo Basin, and the fate of the Congolese tropical forest, can be advanced.

Acknowledgements: Support for this work through NSF Award #1939880 is gratefully acknowledged. We also greatly appreciate the efforts of the ERA5 team at the ECMWF, which made this analysis possible.

References

Balsamo, G., Viterbo, P., Beljaars, A., van den Hurk, B., Hirschi, M., Betts, A. K. and Scipal, K. (2009). A revised hydrology for the ECMWF model: Verification from field site to terrestrial water storage and impact in the Integrated Forecast System. J. Hydrometeorol., 10, 623–643.

Betts AK, Chan DZ, Desjardins RL (2019) Near-Surface Biases in ERA5 Over the Canadian Prairies. *Frontiers in Environmental Science* **7** https://DOI=10.3389/fenvs.2019.00129

Christensen, J., et al. (2013), Climate phenomena and their relevance for future regional climate change, in *Climate Change 2013: The Physical Science Basis. Contribution of Working Group I to the Fifth Assessment Report of the Intergovernmental Panel on Climate Change*, edited by T. Stocker et al., pp. 1217–1308, Cambridge Univ. Press, Cambridge, U. K., and New York.

Cook, K. H., and E. K. Vizy, 2015: Detection and analysis of an amplified warming of the Sahara Desert. *J. Climate,* **28**, 6560-6580.

Cook KH, Vizy EK (2016) The Congo Basin Walker Circulation: Dynamics and connections to precipitation, *Climate Dynamics*, **47**, 1-21. https://doi.org/10.1007/s00382-015-2864-y

Cook, K. H., and E. K. Vizy, 2019: Contemporary climate change of the African monsoon systems. *Current Climate Change Reports*, 5, 145-159. https://doi.org/10.1007/s40641-019-00130-1

Cook KH, Liu Y, Vizy EK (2020) Congo Basin drying associated with poleward shifts of African thermal lows. *Climate Dynamics*, **54**, 863-883. https://doi.org/10.1007/s00382-019-05033-3

Creese A., and R. Washington, 2016: Using qflux to constrain modeled Congo Basin rainfall in the CMIP5 ensemble. *J Geophys Res* **121**, 13415-13442. https://doi.org/10.1002/2016JD025596

Creese A, Washington, 2018: A process-based assessment of CMIP5 rainfall in the Congo Basin: The September-November rainy season. *J Climate,* **31**: 7417-7439. https://doi.org/10.1175/JCLI-D-17-0818.1

Crowhurst DM, Dadson SJ, Washington R (2020). Evaluation of evaporation climatology for the Congo Basin wet seasons in 11 global climate models. *Journal of Geophysical Research: Atmospheres*, *125*, e2019JD030619. https://doi.org/10.1029/2019JD030619

Crowhurst D, Dadson S, Peng J, Washington R (2021) Contrasting controls on Congo Basin evaporation at the two rainfall peaks. *Climate. Dyn*. **56**, 1609-1624.

Danso DK, Anquetin S, Diedhiou A, Lavaysse C, Kobea A, Touré NE (2019) Spatio-temporal variability of cloud cover types in West Africa with satellite-based and reanalysis data. Q J Roy Meteorol Soc 145: 3715-3731. https://doi.org/10.1002/qj.3651

Dargie, G.C., Lawson, I.T., Rayden, T.J., Miles, L., Mitchard, E.T.A., Page, S.E., Bocko, Y. E., Ifo, S.A., Lewis, S.L. (2019) Congo Basin peatlands: threats and conservation priorities. Mitig Adapt Strateg Glob Change 24 (4), 669–686. https://doi.org/ 10.1007/s11027-017-9774-8.

Dezfuli, A.K., and S.E. Nicholson, 2013: The relationship of rainfall variability in western equatorial Africa to the tropical oceans and atmospheric circulation. Part II: The boreal autumn. *J Climate*, **26**, 66-84. https://doi.org/10.1175/JCLI-D-11-00686.1

Dinku T, Funk C, Peterson P, Maidment R, Tadesse T, Gadain H, Ceccato P (2018) Validation of the CHIRPS satellite rainfall estimates over eastern Africa. *Quart. J. Roy. Meteorol. Soc*., **144**, 292-312.

Dyer, E.L.E., D.B. Jones, J. Nusbaumer, H. Li, O. Collins, G. Vettoretti, and D. Noone, 2017: Congo Basin precipitation: Assessing seasonality, regional interactions, and sources of moisture. *J Geophys Res* 122, 6882-6898. https://doi.org/10.1002/2016JD026240

Funk, C., P. Peterson, M. Landsfeld, D. Pedreros, J. Verdin, S. Shukla, G. Husak, J. Rowland, L. Harrison, A. Hoell, and J. Michaelsen, 2015: The climate hazards infrared precipitation with stations – a new environmental record for monitoring extremes. *Scientific Data*, **2**, 150066. https://doi.org/10.1038/sdata.2015.66

Guan, K., M. Pan, L. Haiban, and co-authors, 2015: Photosynthetic seasonality of global tropical forests constrained by hydroclimate. *Nature Geoscience*, **8**, 284-289.

Harrison IJ, Brummett RE, Stiassny MLJ (2016) Congo River Basin. In The Wetland Book, Central African Regional Program for the Environment (USAID). https://doi.org/10.1007/978-94-007-6173-5_92-2

Herrmann SM, Mohr KI (2011) A continental-scale classification of rainfall seasonality regimes in Africa based on gridded precipitation and land surface temperature products. *J. Appl. Meteorol. And Clim.* **50**, 2504-2513.

Hersbach H, Bell B, Berrisford P, Hirahar H, and co-authors (2020) The ERA5 global reanalysis. *Quart. J. Royal Meteorol. Soc*., **146**, 1999-2049.

Howard E, Washington R (2018) Characterizing synoptic expression of the Angolan low. J Climate 31: 7147-7165. https://doi.org/10.1175/JCLI-D-18-0017.1

Huffman, G.J., R.F. Adler, D.T. Bolvin,G. Gu, E.J. Nelkin, K.P. Bowman, Y. Hong, E.F. Stocker, D.B. Wolff, 2007: The TRMM multisatellite precipitation analysis (TMPA): quasi-global, multiyear, combined-sensor precipitation estimates at fine scales. *J Hydrometeorol,* **8**, 38–55. https://doi.org/10.1175/JHM560.1

Huffman, G., D. Bolvin, D. Braithwaite, K. Hsu, R. Joyce, C. Kidd, E.J. Nelkin, S. Sorooshian, J. Tan, and P. Xie, 2018: Algorithm Theoretical Basis Document (ATBD) Version 5.2 NASA Global Precipitation Measurement (GPM) Integrated Multi-satellitE Retrievals for GPM (IMERG). https://pmm.nasa.gov/sites/default/files/document_files/IMERG_ATBD_V5.2_0.pdf

Johannsen F, Ermida S, Martins JPA, Trigo IF, Nogueira M, Dutra e (2019) Cold Bias of ERA5 Summertime Daily Maximum Land Surface Temperature over Iberian Peninsula. *Remote Sens.* **11**, 2570. https://doi.org/10.3390/rs11212570

Joyce, R. J., J. E. Janowiak, P. A. Arkin, and P. Xie, 2004: CMORPH: A method that produces global precipitation estimates from passive microwave and infrared data at high spatial and temporal resolution. *J. Hydromet*., **5**, 487-503. https://doi.org/10.1175/1525-7541(2004)005<0487:CAMTPG>2.0.CO;2

Knoben WJM, Woods RA, Freer JE (2019) Global bimodal precipitation seasonality: A systematic overview. *Int. J. Clim*. **39**, 558-567.

Laing, A.G., R.E. Carbone, and V. Levizzani, 2011: Cycles and propagation of deep convection over Equatorial Africa. *Mon Wea Rev*, **139**, 2832-2853. https://doi.org/10.1175/2011MWR3500.1

Lavaysse C, Flamant C, Janicot S, Parker DJ, LaforeJP, Sultan B, Pelon J (2009) Seasonal evolution of the West African heat low: A climatological perspective. Climate. Dyn. 33, 313-330. https://doi.org/10.1007/s00382-009-0553-4

Longandjo GT, Rouault M (2020) On the structure of the regional-scale circulation over central Africa: Seasonal evolution, variability, and mechanisms. *J. Climate*, **33**, 145 – 162. https://doi.org/10.1175/JCLI-D-19-0176.s1.

Mahli, Y., and J. Wright, 2004: Spatial patterns and recent trends in the climate of tropical rainforest regions. *Phil. Trans. R. Soc. Lond. B*, **359**, 311-329.

Maidment, R. I., R.P. Allan, and E. Black, 2015. Recent observed and simulated changes in precipitation over Africa. *Geophysical Research Letters*, **42**, 8155-8164.

Maidment, R.I., D. Grimes, E. Black, E. Tarnavsky, M. Young, H. Greatrex, R.P. Allan, T. Stein, E. Nkonde, S. Senkunda and E. Misael Uribe Alcántara, 2017: A new, long-term daily satellite-based rainfall dataset for operational monitoring in Africa, *Scientific Data*, **4**, 170063. https://doi.org/10.1038/sdata.2017.63

Mueller B, Hirschi M, Jimenez C et al (2013) Benchmark products for land evapotranspiration: landFlux-EVAL multi-data set synthesis. Hydrol Earth Syst Sci 17:3707–3720. https ://doi.org/10.5194/hess-17-3707-2013

Nicholson SE, Grist JP (2003) The seasonal evolution of the atmospheric circulation over West Africa and equatorial Africa. *J. Climate,* **16**, 1013-1030.

Nicholson SE, Klotter D, Dezfuli AK, Zhou L (2018) New rainfall datasets for the Congo basin and surrounding regions, *J. Hydrometeor*., **19**, 1379-1396.

Novella NS, Thiaw WM (2013) African rainfall climatology version 2 for famine early warning systems. *J. Appl. Meterol. Climatology*, **52**, 588-606.

Pokam, W. M., L. A. T. Djiotang, and F. K. Mkankam, 2012: Atmospheric water vapor transport and recycling in equatorial Central Africa through NCEP/NCAR reanalysis data. Climate Dyn., 38, 1715–1729, https://doi.org/10.1007/s00382-011-1242-7

Pokam, WM, Bain CL, Chadwick RS, Graham R, Sonwa DJ, Kamga FM (2014) Identification of processes driving low level westerlies in west equatorial Africa. *J. Climate*, **27**, 4245–4262, https://doi.org/10.1175/JCLI-D-13-00490.1

Schwendike JP, Govekar P, Reeder MJ, Wardle R, Berry GJ, Jakob C (2014) Local partitioning of the overturning circulation in the tropics and the connection to the Hadley and Walker circulations, *J. Geophys. Res. Atmos.*, **119**, 1322–1339, https://doi:10.1002/2013JD020742.

Shapiro AC, Grantham HS, Aguilar-Amuchastegui N, Murray NJ, Gond V, Rickenbach O (2021) Forest condition in the Congo Basin for the assessment of ecosystem conservation status. Ecological Indicators 122 (107268) https://doi.org/10.1016/j.ecolind.2020.107268

Sori, R, Nieto R, Vicente-Serrano SM, Drumond A, Gimeno L (2017) A Lagrangian perspective of the hydrological cycle in the Congo River basin. *Earth Syst. Dyn*., **8**, 653-675.

Sorooshian, S., K.-L. Hsu, X. Gao, H.V. Gupta, B. Imam, and D. Braithwaite, 2000: Evaluation of PERSIANN system satellite-based estimates of tropical rainfall. *Bull Amer Meteorol Soc*, **81**, 2035-2046. https://10.1175/1520-0477(2000)081<2035:EOPSSE>2.3.CO;2

Sun, X.M., Cook, K. H., and E. K. Vizy, 2017: The South Atlantic subtropical high: Climatology and interannual variability. *Climate Dynamics*, 30, 3279-3296. https://journals.ametsoc.org/doi/10.1175/JCLI-D-16-0705.1

Tamoffo AT, Dosio A, Vondou DA, Sonkoue D (2020) Process-based analysis of the added value of dynamical downscaling over central Africa. Geophys. Res. Lett., 47. https://doi.org/10.1029/2020GL089702

Van der Ent RJ, Savenie HHG (2013) Oceanic sources of continental precipitation and the correlation with sea surface temperature. *Water. Resource Res*., **49**, 3993-4004.

Viterbo P, Beljaars ACM (1995). An improved land surface parametrization scheme in the ECMWF model and its validation. ECMWF Tech. Report No. 75, Research Department.

Vizy EK, Cook KH (2009) A mechanism for African monsoon breaks: Mediterranean cold air surges. J. Geophys. Res., 114, D01104, doi:10.1029/2008JD010654.

Vizy EK, Cook KH (2014) Impact of cold air surges on rainfall variability in the Sahel and wet African tropics: a multi-scale analysis. *Clim. Dyn*., 43, 1057-1081.

Vizy EK, Cook KH (2017) Seasonality of the observed amplified Sahara warming trend and implications for Sahel rainfall. *J. Climate*, **30**, 3073-3094

Vizy EK, Cook KH (2019) Observed relationship between the Turkana low-level jet and boreal summer convection. Clim. Dyn 53: 4037 – 4058. https://doi.org/10.1007/s00382-019-04769-2

Washington, R., R. James, H. Pearce, W.M. Pokam, and W. Moufouma-Okia, 2013: Congo rainfall climatology: can we believe the climate models? *Philosophical Transactions of the Royal Society B*, **368**: 20120296.

Zhao S, Cook KH (2020) Influence of Walker circulations on East African rainfall. *Climate Dynamics*, **56**, 2127-2147. https://doi.org/10.1007/s00382-020-05579-7

Zhou, L.M., Y.H. Tian, R.B. Myneni, P. Ciais, S. Saatchi, Y.Y. Liu, S.L. Piao, H.S. Chan, E.F. Vermote, C.H. Song, et al., 2014: Widespead decline of Congo rainforest greenness in the past decade. *Nature*, **509**, 86-89.

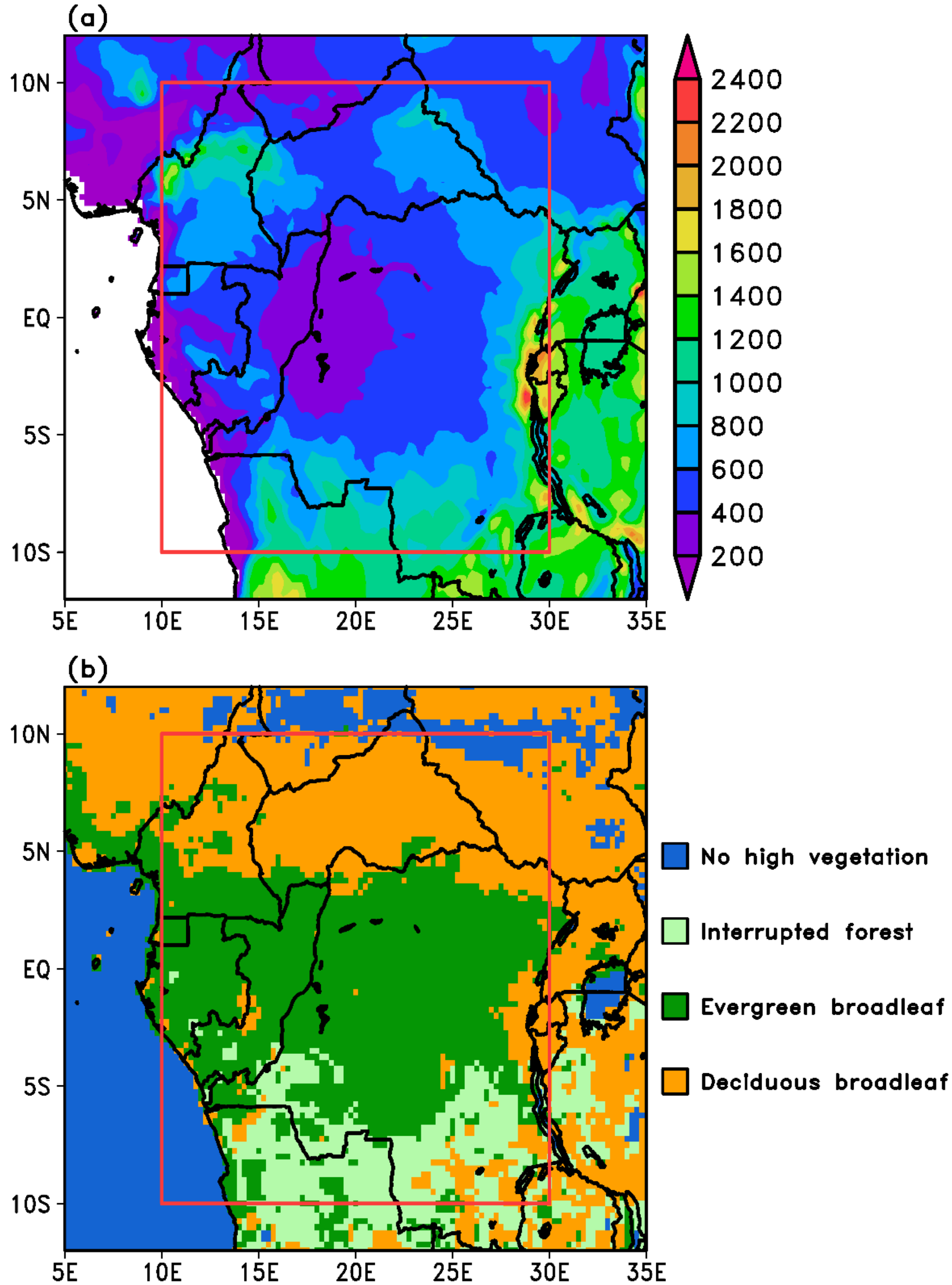

Figure 1. (a) Topography of equatorial Africa (shaded; m). (b) Specification of the high vegetation type in the ERA5 reanalysis. Red boxes in (a) and (b) denote the primary analysis region.

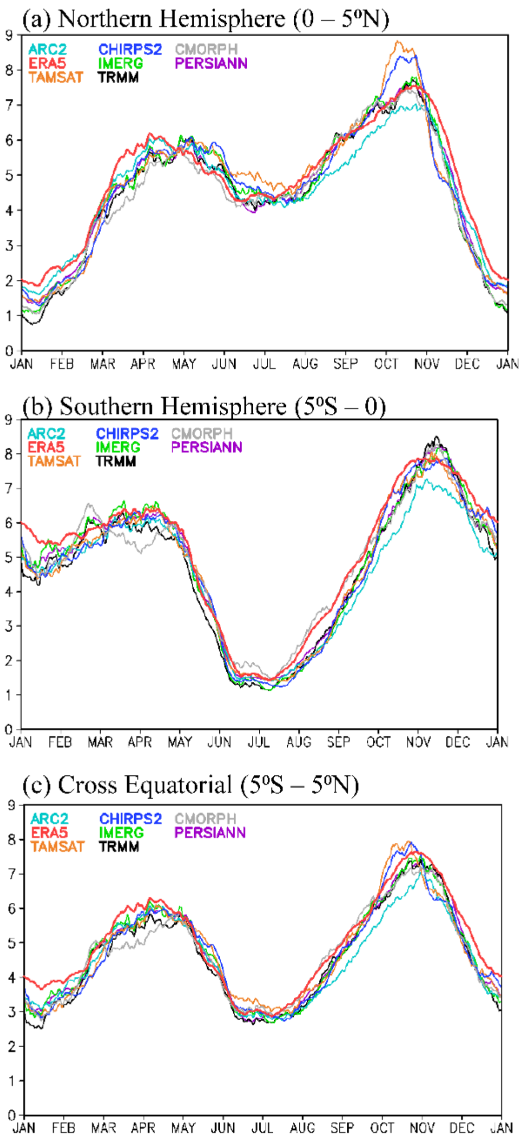

Figure 2. Daily precipitation climatology (mm/day) for various datasets and the ERA5 reanalysis averaged from 10ºE-30ºE and (a) 0º-5ºN, (b) 5ºS-0º, and (c) 5ºS-5ºN. A 12-day running mean smoothing has been applied

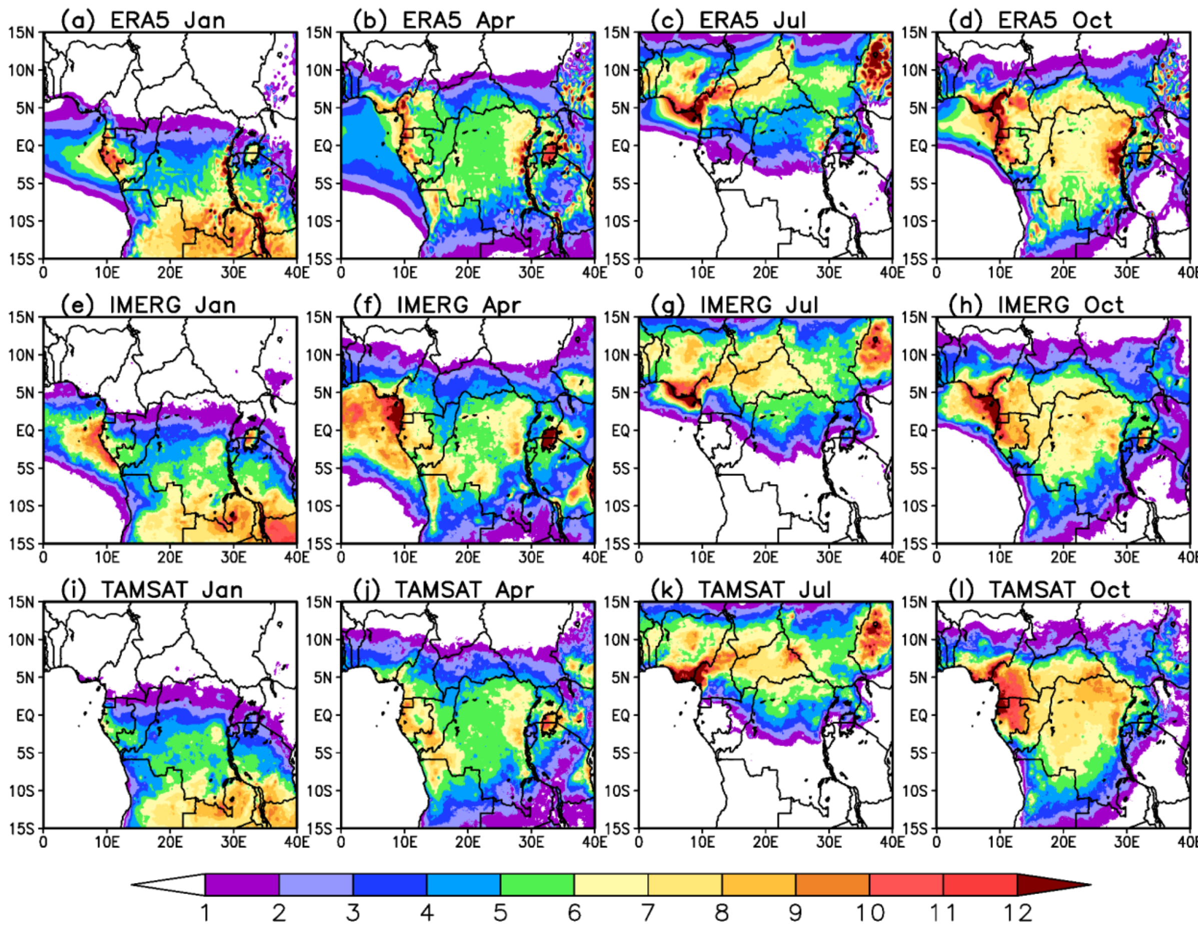

Figure 3. Precipitation distributions (mm/day) for months with maximum and minimum rainfall for the (a)-(d) ERA5, (e)-(h) IMERG, and (i)-(l) TAMSAT climatologies.

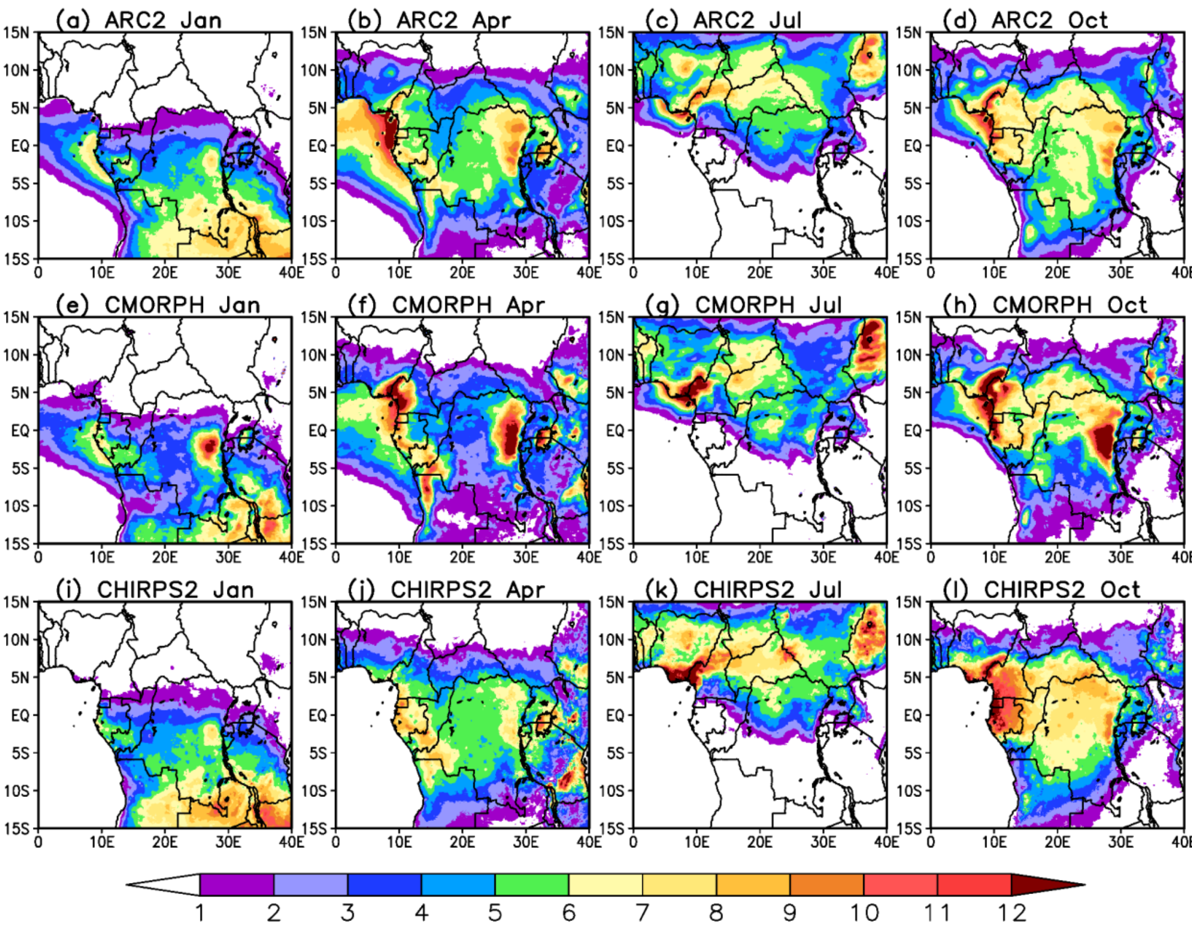

Figure 4. Precipitation distributions (mm/day) for months with maximum and minimum rainfall for the (a)-(d) ARC2, (e)-(h) CMORPH, and (i)-(l) CHIRPS2 climatologies.

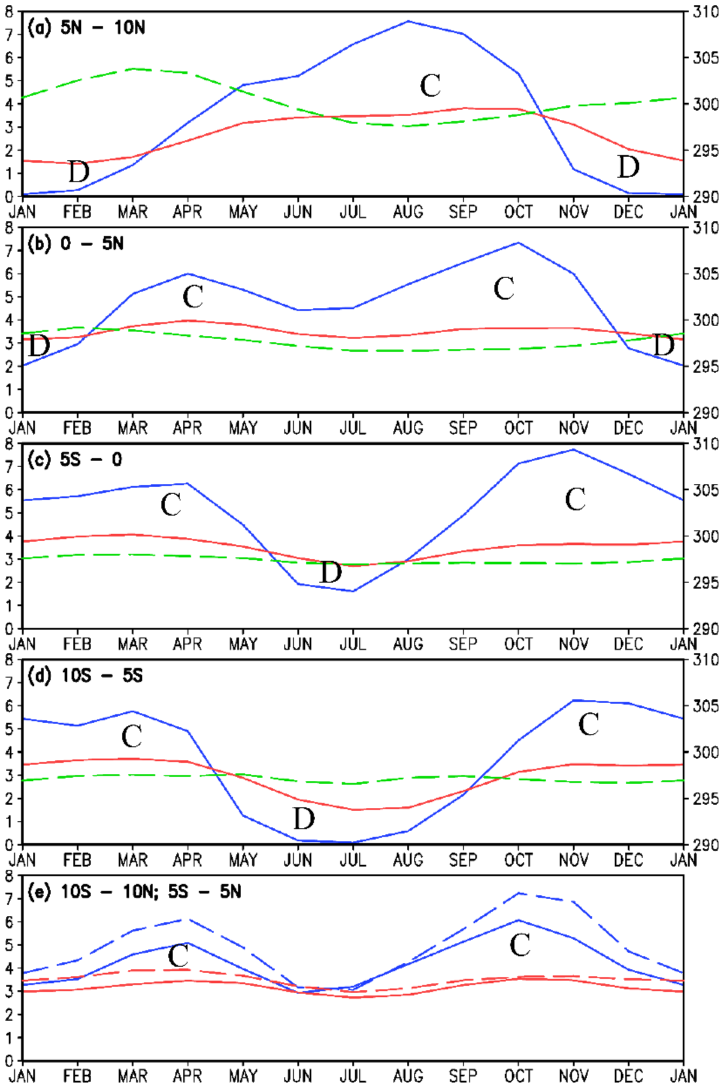

Figure 5. Monthly mean precipitation (blue solid line), evapotranspiration (red solid line), and skin temperature (green dashed line) from the ERA5 climatology averaged from 10ºE to 30ºE and (a) 5ºN – 10ºN, (b) 0º – 5ºN, (c) 5ºS – 0º, (d) 10ºS – 5ºS, and (e) 10ºS – 10ºN with 5ºS-5ºN dashed. Units are mm/day for precipitation and K for temperature. *C* and *D* indicate regions of vertically integrated moisture convergence and divergence.

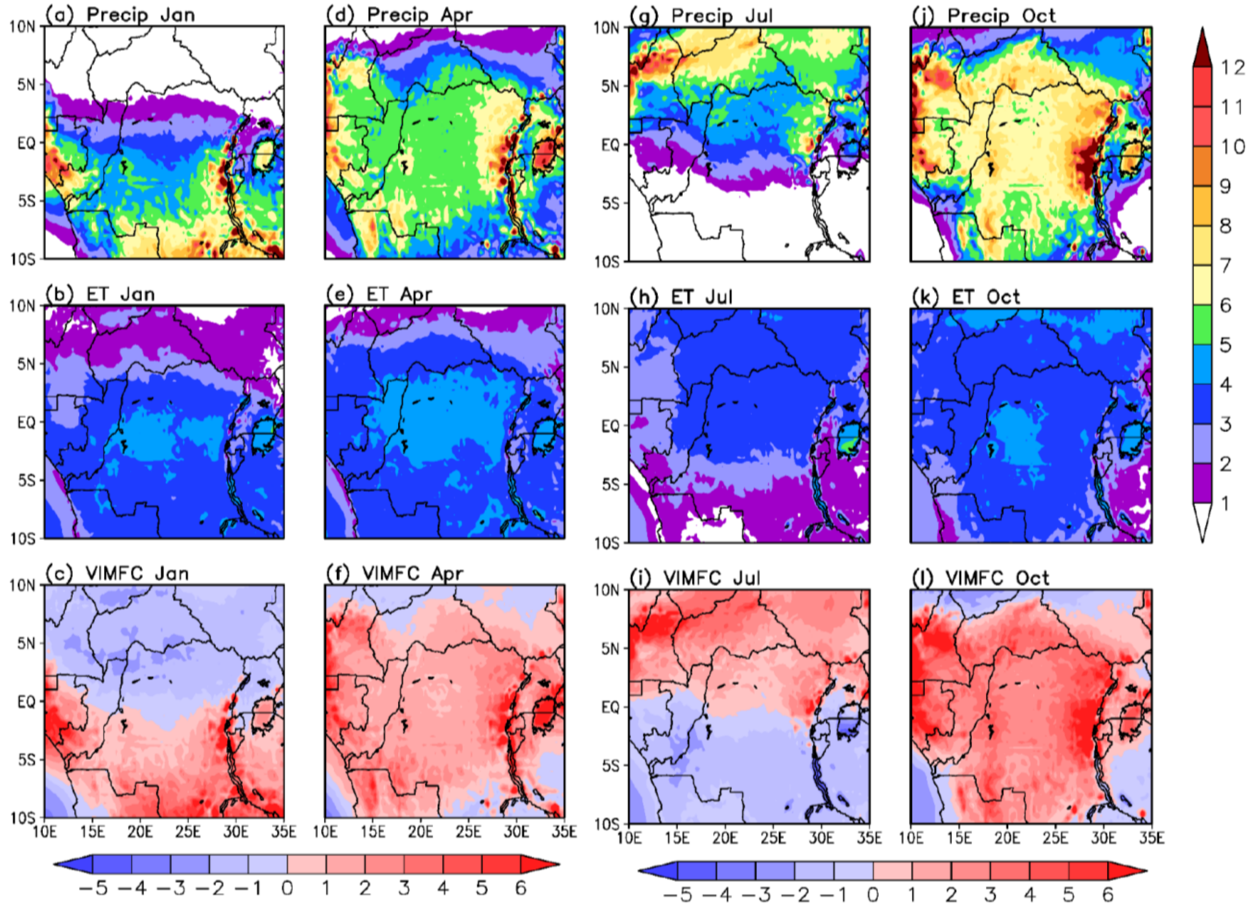

Figure 6. January (a) precipitation, (b) evapotranspiration, and (c) vertically-integrated moisture flux convergence from the ERA5 climatology. April (d) precipitation, (e) evapotranspiration, and (f) vertically-integrated moisture convergence. July (g) precipitation, (h) evapotranspiration, and (i) vertically-integrated moisture convergence. October (j) precipitation, (k) evapotranspiration, and (l) vertically-integrated moisture convergence. Units are mm/day.

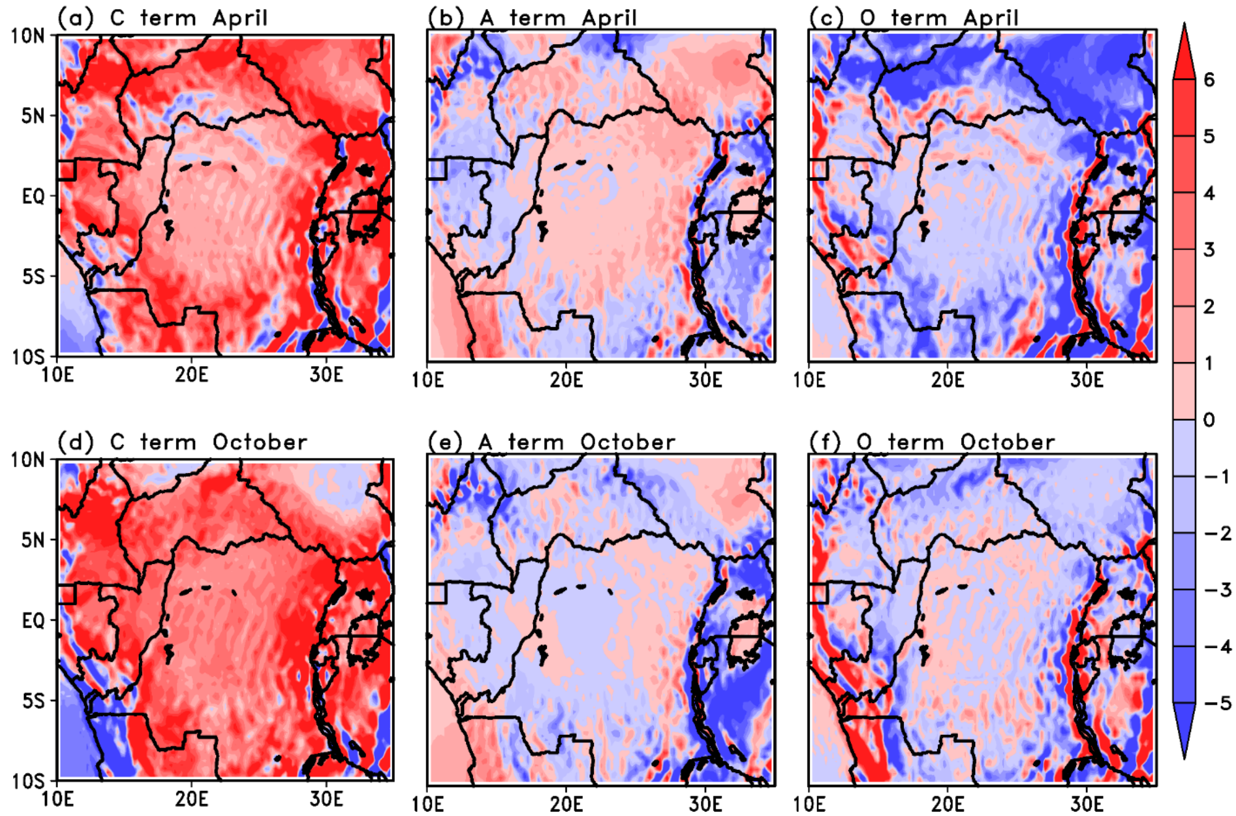

Figure 7. Vertically-integrated convergence (C; Eq. 2), advection (A; Eq. 3), and orographic (O; Eq. 4) components of the vertically-integrated moisture flux convergence during April and October. Units are mm/day.

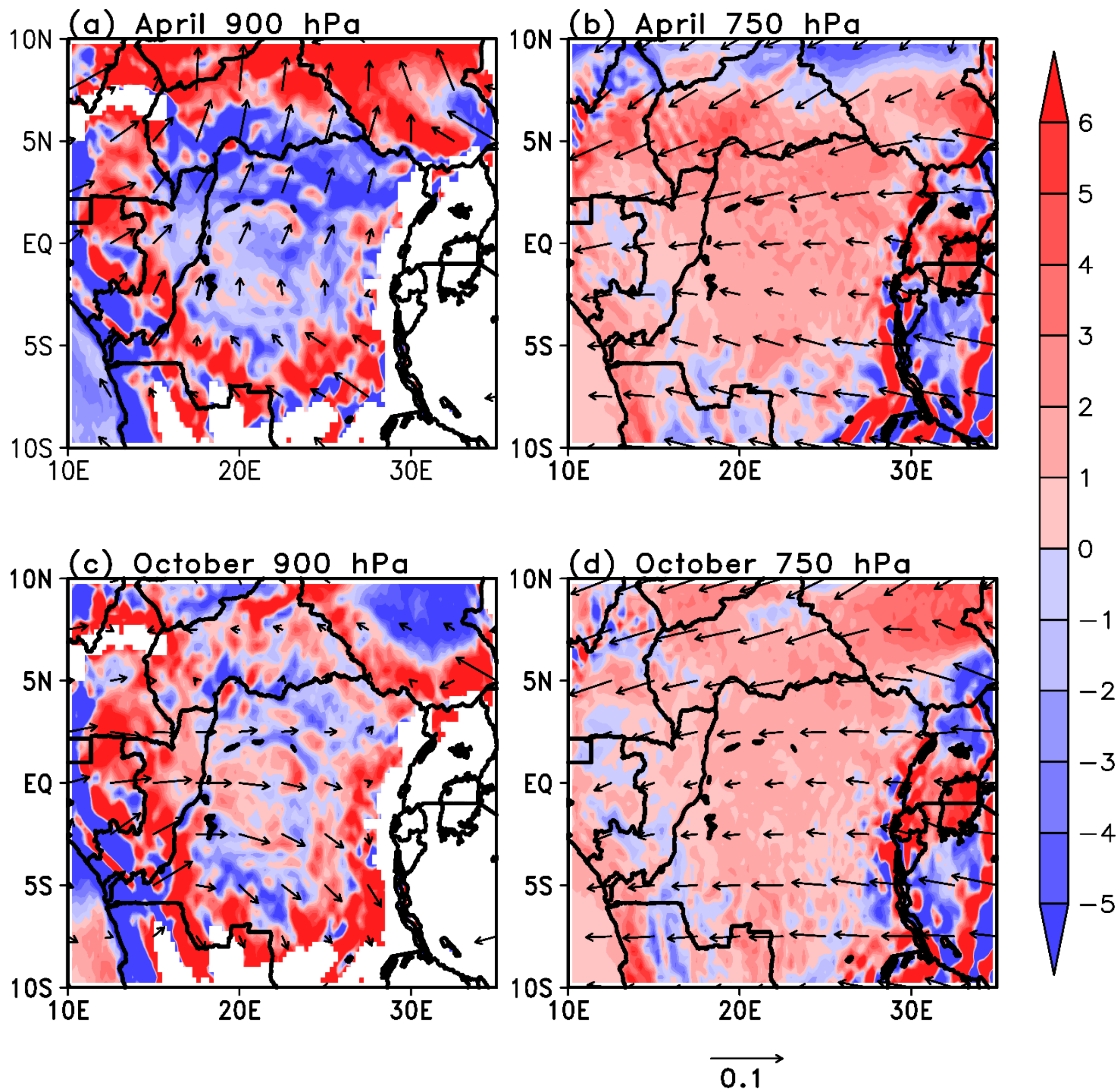

Figure 8. Moisture convergence term ($q\nabla\cdot\vec{V}$; shading; $s^{-1}x10^{-3}$) and moisture transport vectors ($q\vec{V}$; m/s) for April at (a) 900 hPa and (b) 750 hPa. Moisture convergence term and moisture transport vectors for October at (c) 900 hPa and (d) 750 hPa. Color bar applies to all panels, as does the vector scale in m/s on the lower right. White shading indicates where topography exceeds the pressure level plotted.

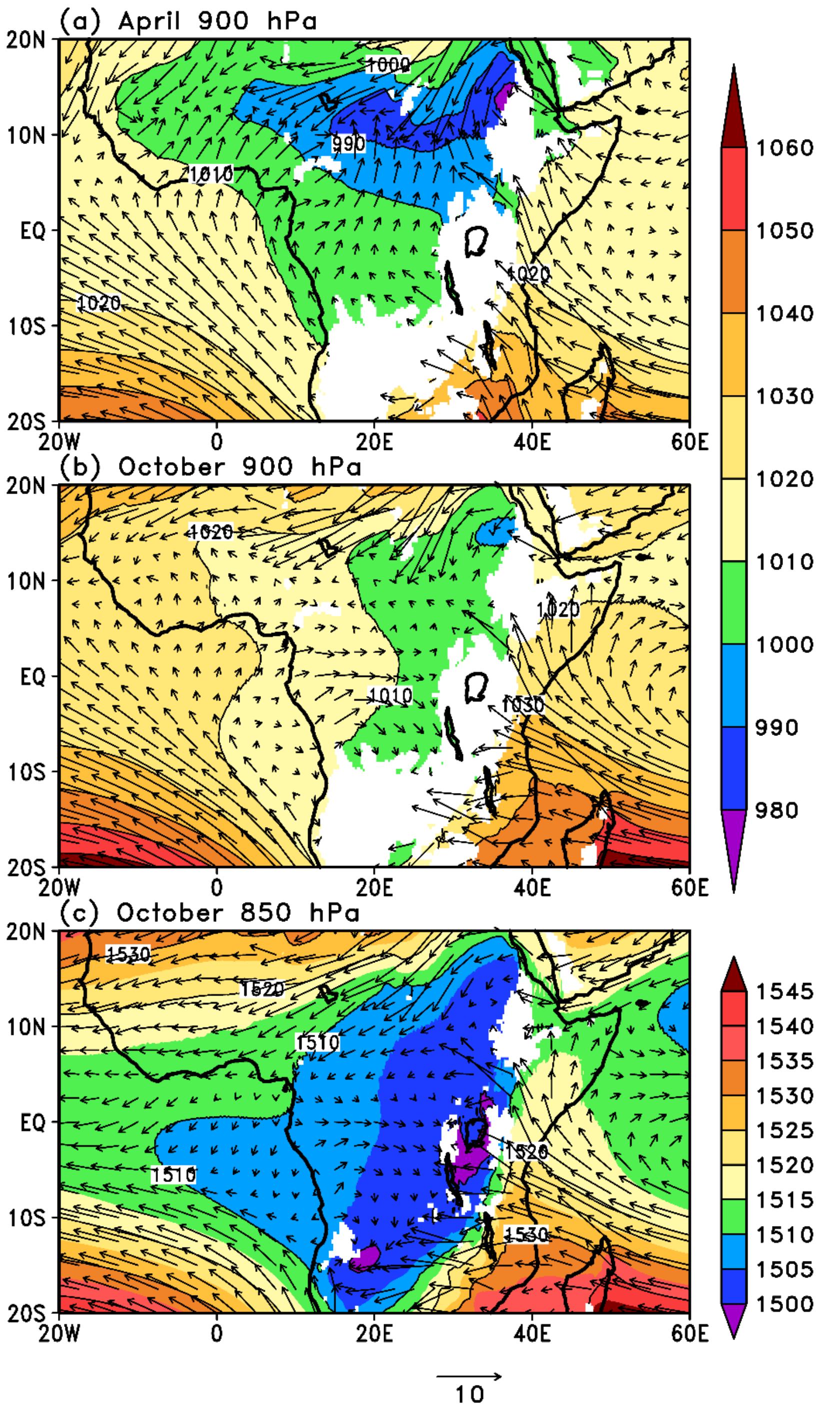

Figure 9. Wind and geopotential height at 900 hPa for (a) April and (b) October. (c) Wind and geopotential height at 850 hPa for October. Vector scale is in m/s, and geopotential heights are in gpm. White shading indicates where topography exceeds the pressure level plotted.

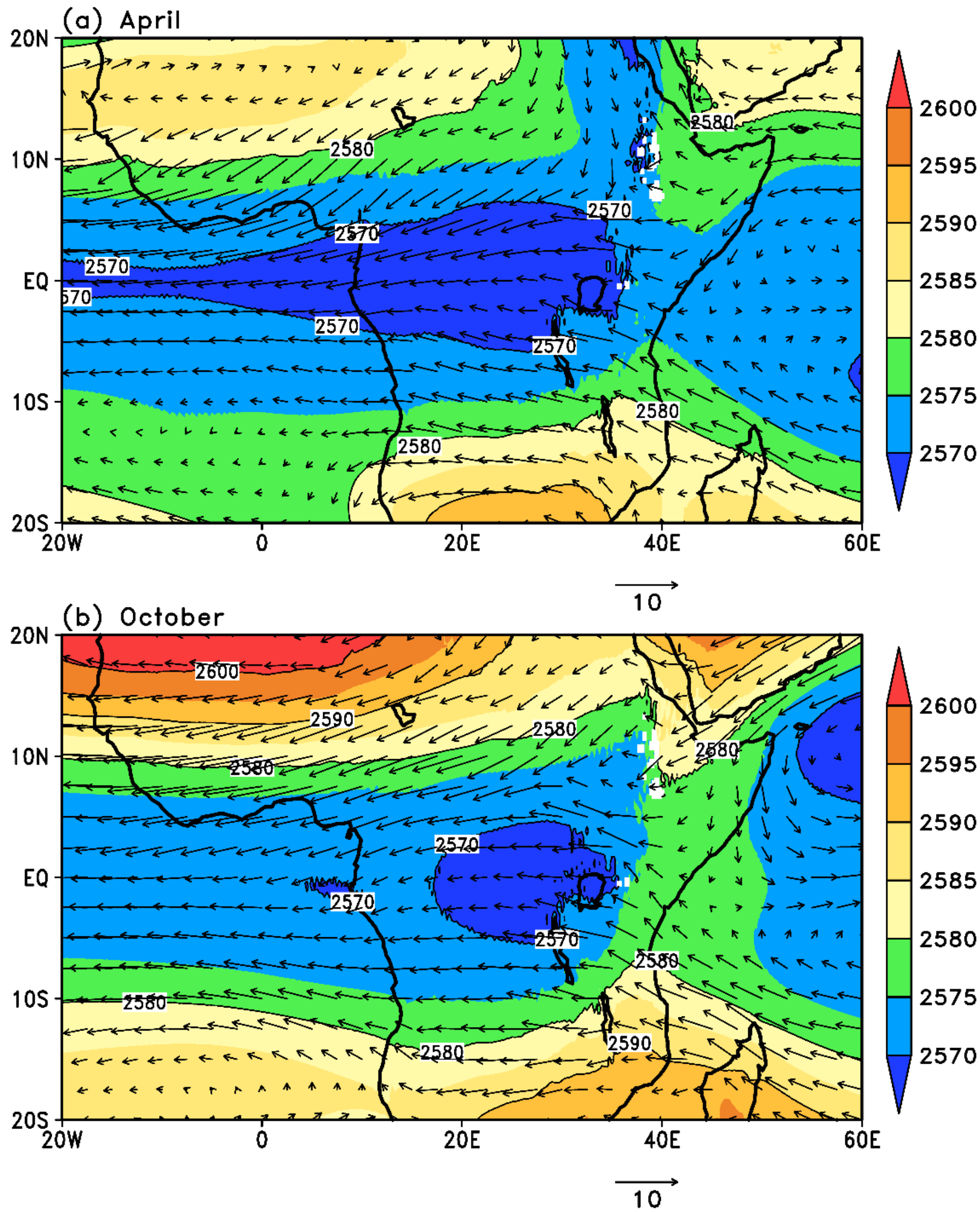

Figure 10. Wind (vectors) and geopotential heights (shaded) at 750 hPa for (a) April and (b) October. Vector scale is in m/s, and geopotential heights are in gpm.

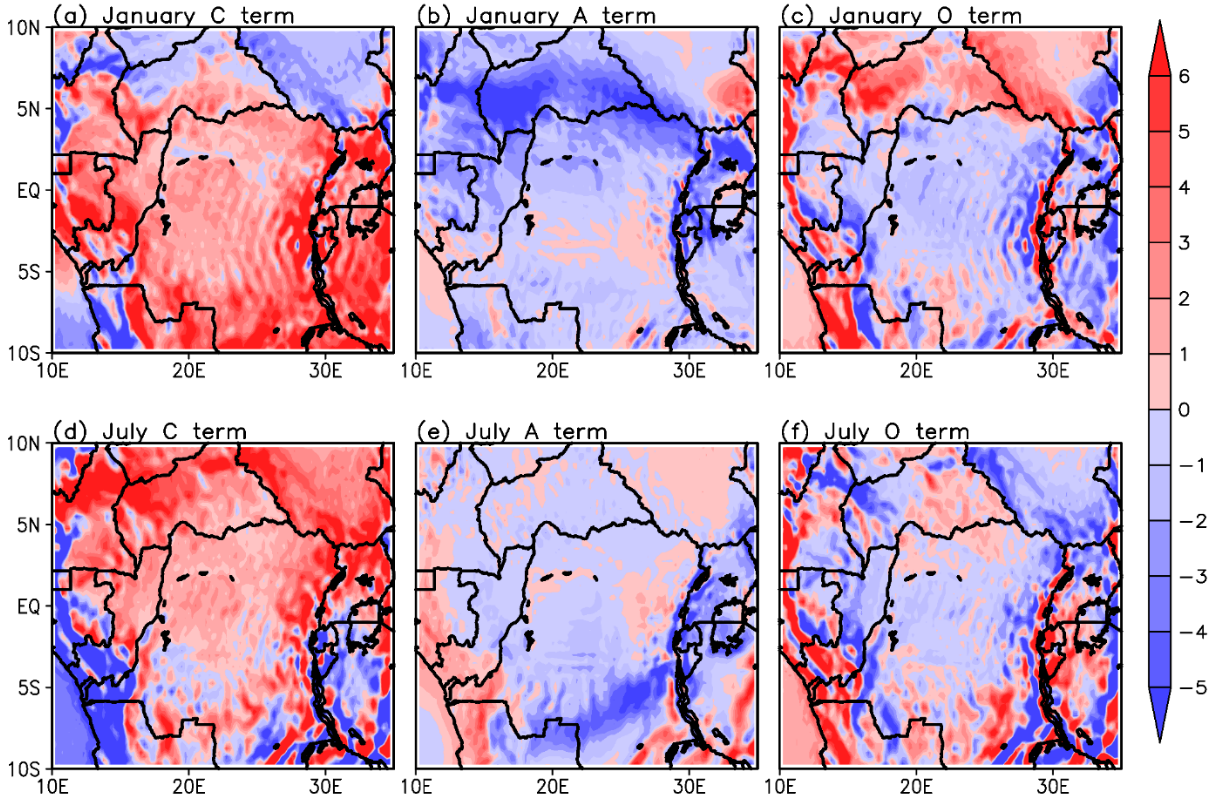

Figure 11. Vertically-integrated convergence (C; Eq. 2), advection (A; Eq. 3), and orographic (O; Eq. 4) components of the vertically-integrated moisture flux convergence during April and October. Units are mm/day.

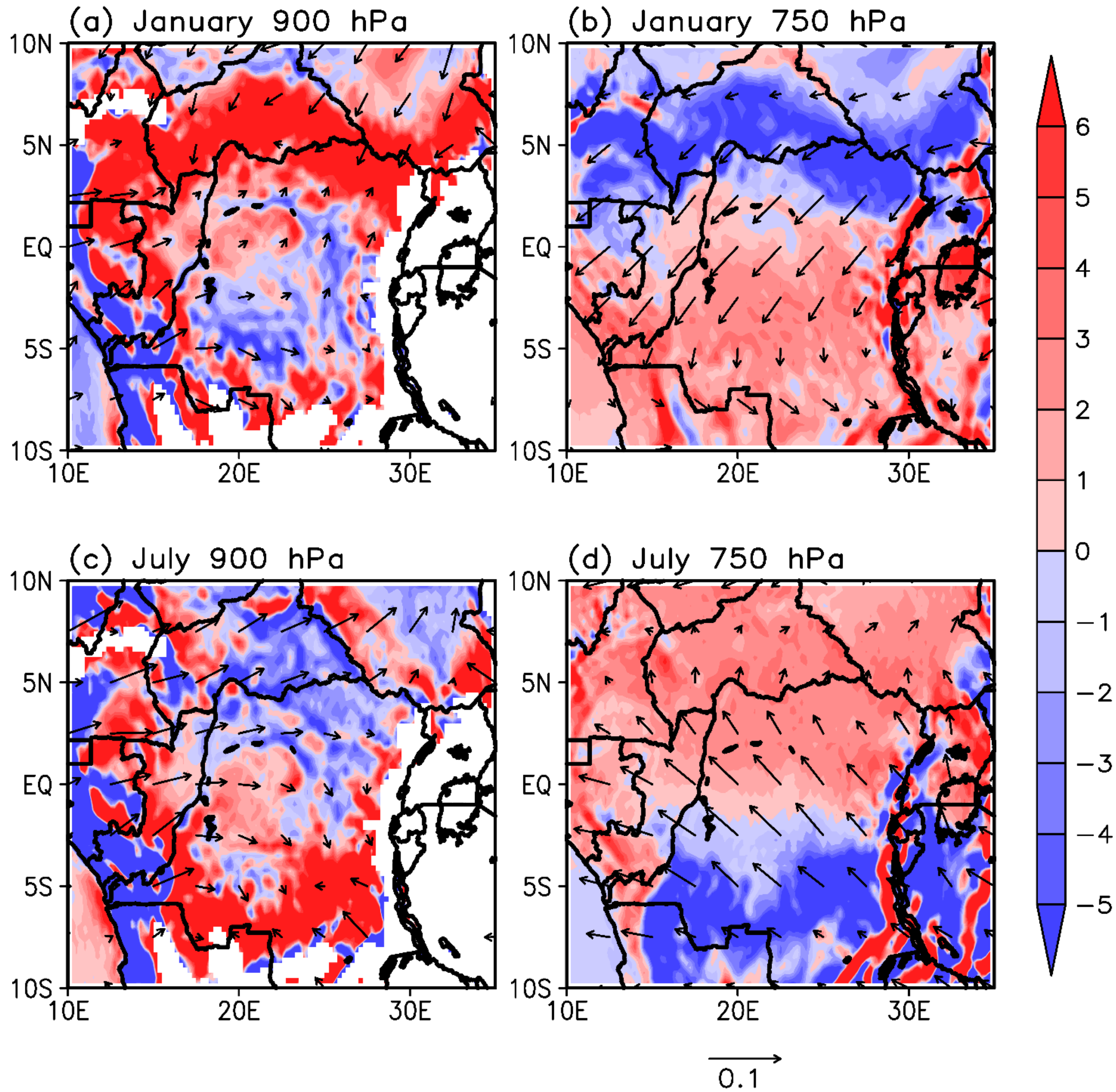

Figure 12. Moisture convergence term (shading; $s^{-1}x10^{-3}$) and moisture transport vectors (m/s) for January at (a) 900 hPa and (b) 750 hPa. Moisture convergence term and moisture transport vectors for July at (c) 900 hPa and (d) 750 hPa. Color bar applies to all panels, as does the vector scale in m/s on the lower right. White shading indicates where topography exceeds the pressure level plotted.

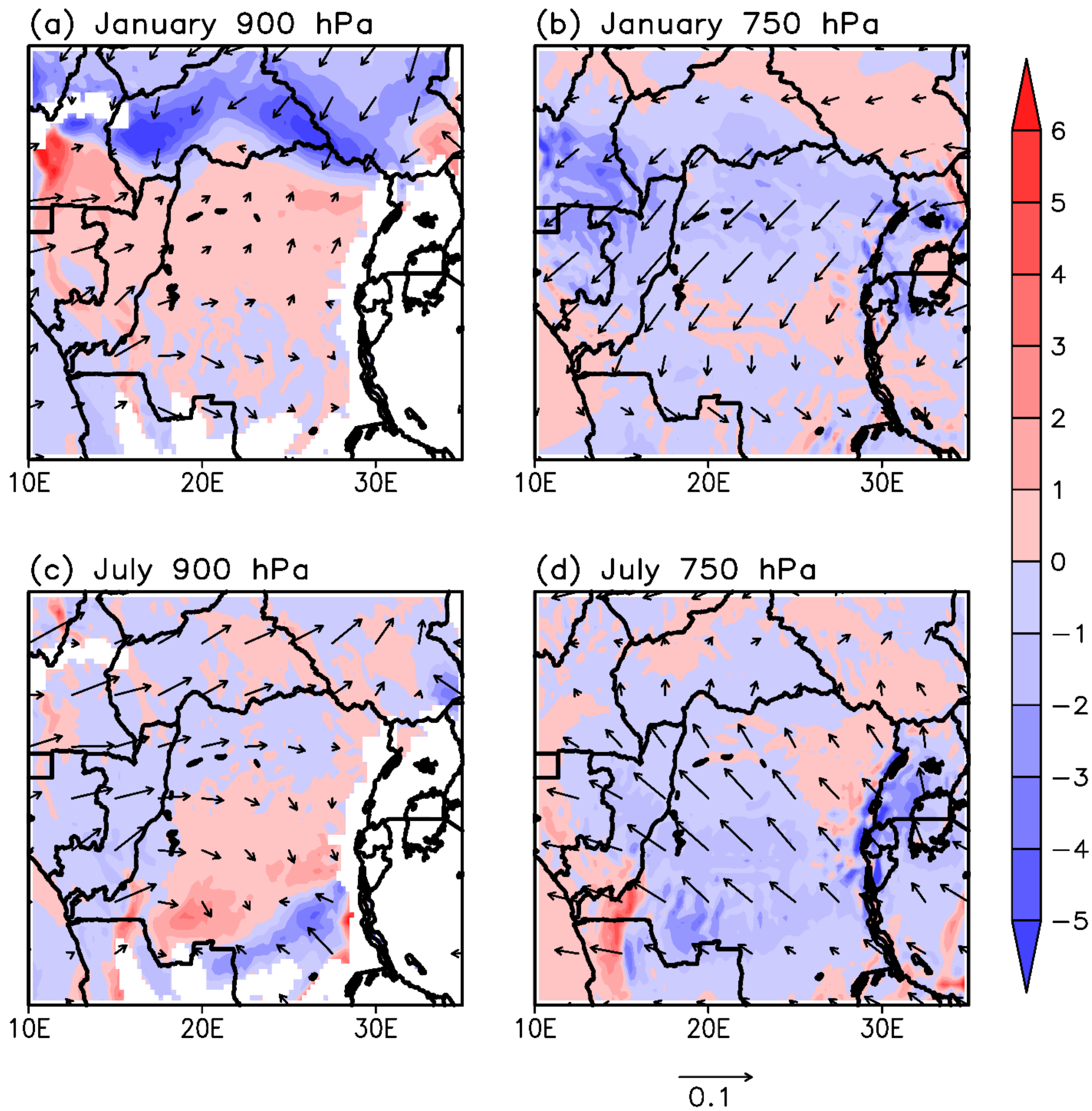

Figure 13. Moisture advection term (shading; $s^{-1}x10^{-3}$) and moisture transport vectors (m/s) for January at (a) 900 hPa and (b) 750 hPa. Moisture advection term and moisture transport vectors for July at (c) 900 hPa and (d) 750 hPa. Color bar applies to all panels, as does the vector scale in m/s on the lower right. White shading indicates where topography exceeds the pressure level plotted.

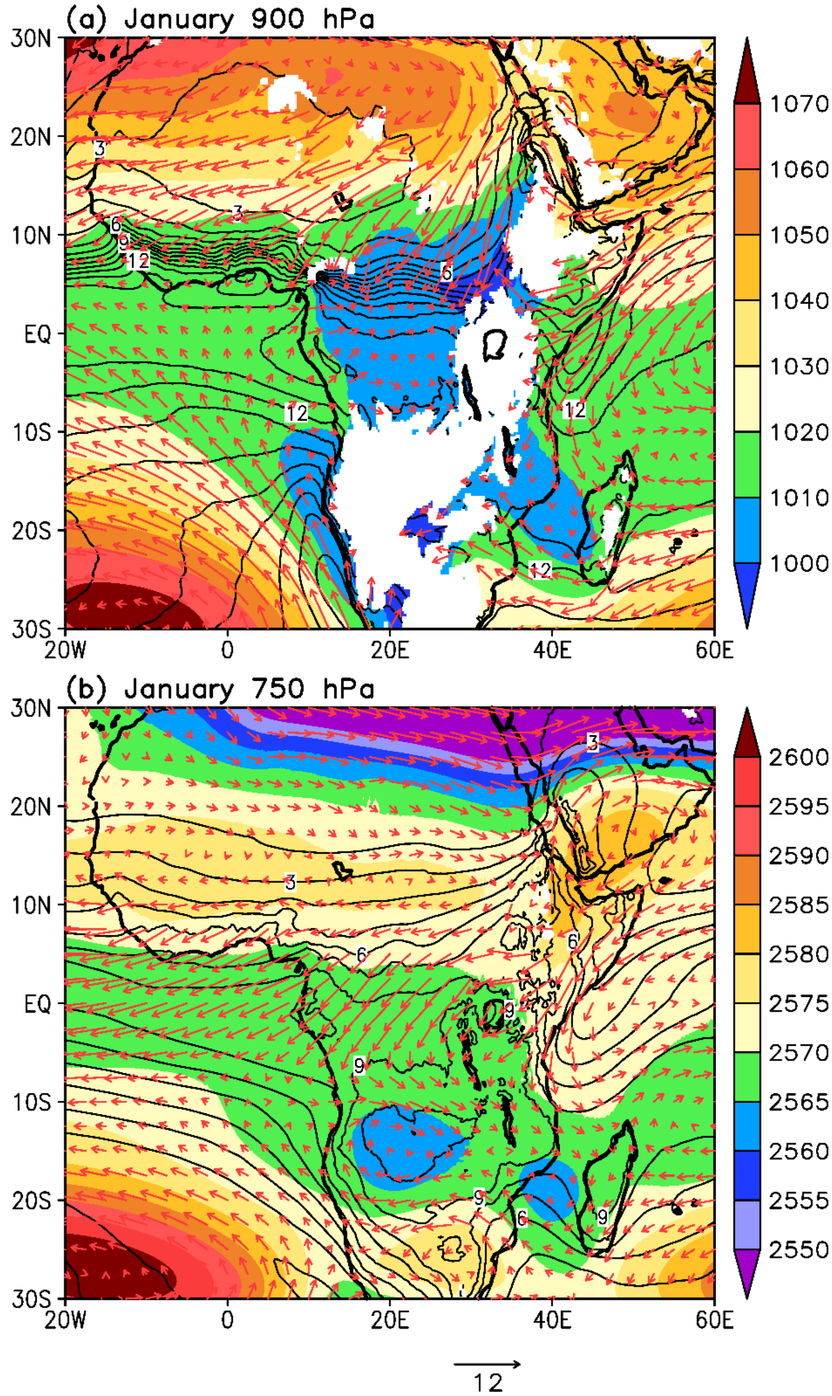

Figure 14. Wind (vectors), geopotential heights (shading), and specific humidity (contours) for January at (a) 900 hPa and (b) 750 hPa. Vector scale is in m/s and applies to both panels; geopotential heights are in gpm. White shading indicates where topography exceeds the pressure level plotted.

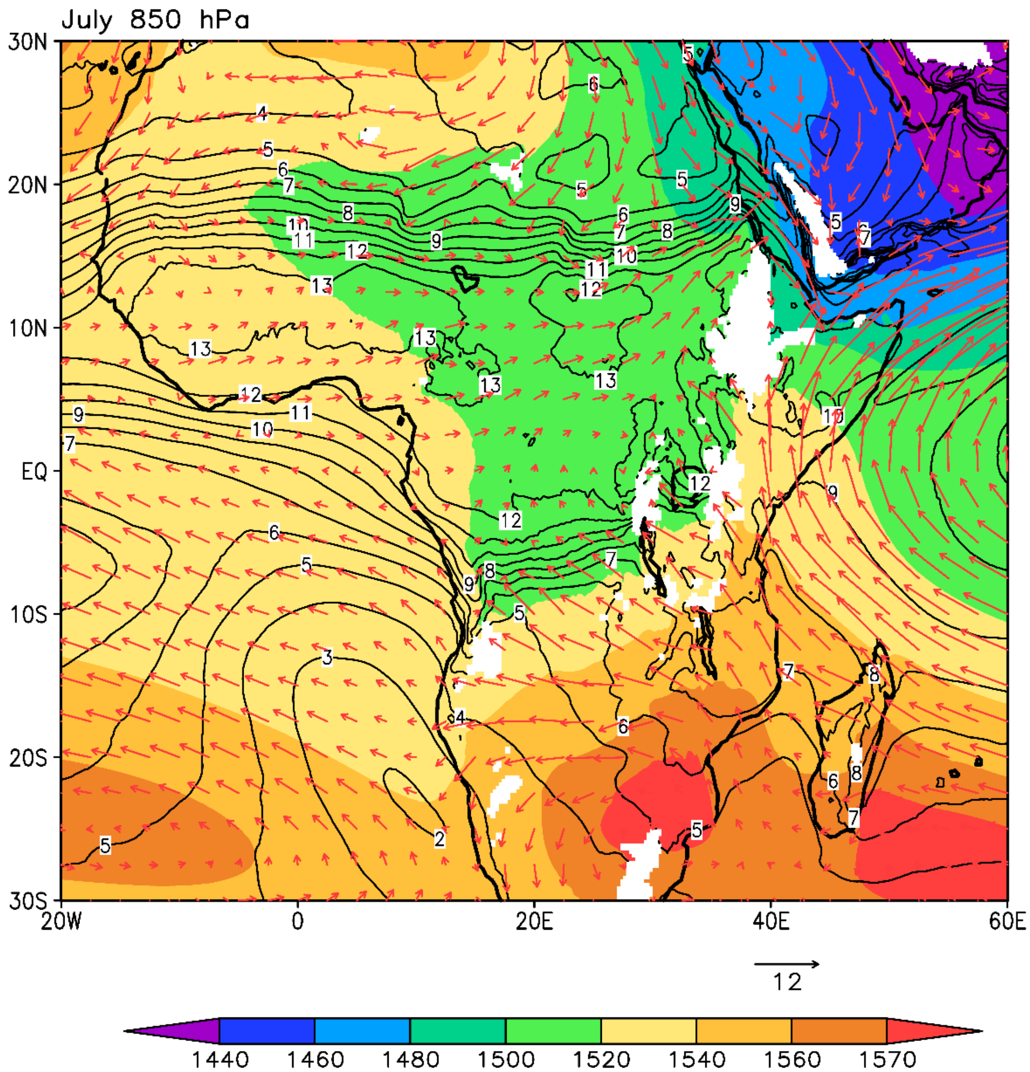

Figure 15. Wind (vectors), geopotential heights (shading), and specific humidity (contours) for July at 850 hPa. Vector scale is in m/s, and geopotential heights are in gpm. White shading indicates where topography exceeds the pressure level plotted.